



Aeroacoustic topology optimization of noise barrier based on Lighthill's acoustic analogy



Ki Hyun Kim, Gil Ho Yoon *

School of Mechanical Engineering, Hanyang University, Seoul, 04763, Republic of Korea

ARTICLE INFO

Article history:

Received 19 February 2020

Received in revised form 3 June 2020

Accepted 9 June 2020

Available online 15 June 2020

Handling Editor: L. Huang

Keywords:

Topology optimization

Aeroacoustic sound source

Lighthill's acoustic analogy

Noise barrier

ABSTRACT

Topology optimization for the shape of noise barrier taking into account the aeroacoustic sound source is presented based on Lighthill's acoustic analogy approach. In the previous acoustic topology optimization based on the Helmholtz equation, only simple acoustic sound sources were taken into account. To overcome this limitation, the present aeroacoustic topology optimization is performed using Lighthill's equation that represents the sound propagation by an aeroacoustic sound source. In this study, aeroacoustic sound sources are randomly generated through the stochastic noise generation and radiation method. As an interpolation method of material properties by continuous design variables, the linear filter and the sigmoid penalty function are used. The top shape of noise barrier is designed by the optimization examples for various conditions, such as random aeroacoustic sound sources, interpolation methods, and target frequencies.

© 2020 Elsevier Ltd. All rights reserved.

1. Introduction

This study investigates aeroacoustic topology optimization for the top shape of noise barrier through Lighthill's acoustic analogy approach. Previous research on topology optimization in acoustic problems has dealt with simple acoustic sound sources such as a monopole sound or a plane wave sound. In contrast, present study deals with aeroacoustic sound sources generated from turbulent flow. In other words, present study is the expansion of topology optimization from the acoustic problem to the aeroacoustic problem. To the best of the authors' knowledge, this type of research has not been attempted to date.

Lighthill's acoustic analogy approach is a hybrid aeroacoustic analysis method that simulates the sound propagation for the pre-generated aeroacoustic sound source. By separating the sound propagation from the sound generation, the aeroacoustic analysis can be achieved by solving an inhomogeneous acoustic wave equation such as Lighthill's equation. Fig. 1 shows a comparison of the previous acoustic topology optimization based on the Helmholtz equation with the present aeroacoustic topology optimization based on Lighthill's equation. Lighthill's equation has an aeroacoustic sound source term on the right side of equation compared to the Helmholtz equation. The left side terms of both equations can be arranged to be identical. Therefore, aeroacoustic topology optimization using Lighthill's equation can be implemented based on the strategies of acoustic topology optimization using the Helmholtz equation.

Topology optimization is an optimization method that optimizes the layout (distribution) of finite materials to design the shape of structure to maximize a performance of interest. When the performance is calculated by the finite element analysis,

* Corresponding author.

E-mail addresses: ghy@hanyang.ac.kr, gilho.yoon@gmail.com (G.H. Yoon).

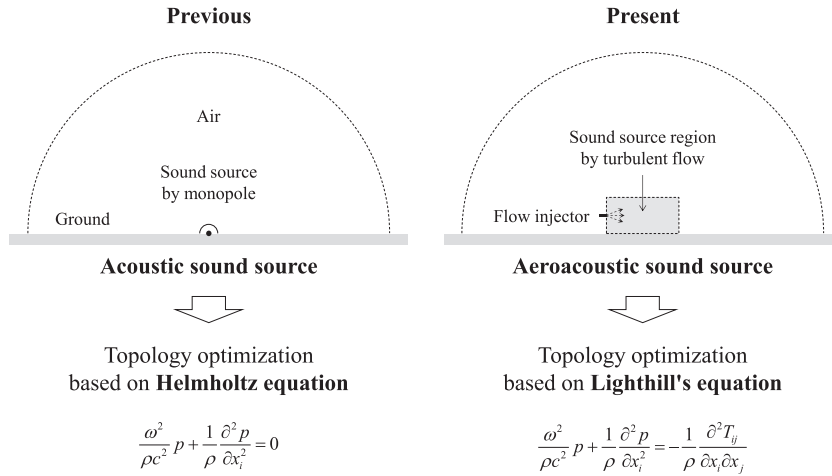


Fig. 1. Comparison of the present aeroacoustic topology optimization with the previous acoustic topology optimization.

the material types of finite elements in the design domain are determined by design variables, resulting in a material layout representing the shape of structure. Therefore, an optimized material layout can be obtained by using optimization algorithms. Topology optimization method was originally developed in structural optimization problems [1] and has been applied to various physics systems [2]. Topology optimization in acoustic problems has been applied to the design of rooms [3–5], noise barriers [5–8], mufflers [9,10], horns [11], metamaterials [12], and so on. These optimization studies performed a numerical analysis based on the Helmholtz equation. The Helmholtz equation was also used in conjunction with other equations for the topology optimization in multiphysics problems [13–16]. Conventional topology optimization in acoustic problems solves a gradient-based optimization problem using continuous design variables based on the solid isotropic material with penalization (SIMP) method. As material properties assigned to finite elements are defined by continuous design variables, the gray element problem related to an undesirable intermediate material state between air and the rigid material can arise. To solve this problem, various filtering techniques were investigated in structural topology optimization [17–19].

In the proposed topology optimization, the design of noise barrier for aeroacoustic sound sources is performed through the finite element analysis of Lighthill's equation. Lighthill's equation simulates sound wave propagation by an aeroacoustic sound source which is calculated from the turbulent flow [20,21]. As a flow simulation method in the present study, the stationary incompressible Reynolds-averaged Navier-Stokes (RANS) equations coupled with the $k-\varepsilon$ turbulence model [22] are solved to obtain the mean flow properties. From the mean flow properties, the fluctuating flow velocity field is randomly synthesized using the stochastic noise generation and radiation (SNGR) method [23]. In relation to the shape of noise barrier [24,25], many researchers applied engineering optimization techniques [26–28] including topology optimization [5–8]. Compared to previous topology optimization studies on noise barriers, the design domain of this study is limited to the top of noise barrier. The top shape of noise barrier plays an important role in the noise reduction performance associated with the diffraction of sound waves. In relation to the gray element problem, material properties are defined by design variables using the linear filter and the sigmoid function [29] to reduce the elements of an intermediate material state in the optimized material layout. The method of moving asymptotes (MMA) algorithm [30] is used to solve the gradient-based optimization problem.

In Section 2, the finite element analysis using Lighthill's equation is provided with the calculation of aeroacoustic sound sources. In Section 3, a topology optimization problem is defined for the design of noise barrier. In Section 4, topology optimization results are presented. Optimized material layouts are investigated for different random aeroacoustic sound sources and various optimization conditions. Finally, in Section 5, the conclusions of this study are given.

2. Finite element analysis using Lighthill's equation

Lighthill's acoustic analogy approach is a hybrid aeroacoustic analysis method to predict flow-induced noise. Compared with the direct method that solves the full compressible Navier-Stokes equations, the hybrid method consists of two analysis steps. In the first step, an aeroacoustic sound source is generated through a flow analysis. In the second step, sound wave propagation for the sound source generated in the first step is computed by an inhomogeneous acoustic wave equation, which is rearranged from the compressible Navier-Stokes equations. With respect to the inhomogeneous equation, Lighthill's equation was first proposed in by Lighthill [20,21]. In the use of Lighthill's equation, it is assumed that the sound source generated from the turbulent flow propagates in a medium at rest or a medium where mean flow has little effect on the sound

wave propagation. This study solves two-dimensional Lighthill's equation in the frequency domain by the finite element method.

2.1. Finite element formulation of Lighthill's equation

Lighthill's equation is derived from the mass and momentum conservation equations of compressible Navier–Stokes equations [31]. The mass conservation equation and its time derivative equation are given by Eq. (1), and the momentum conservation equation and its spatial derivative equation are given by Eq. (2), where the density, the flow velocity, the pressure, and the deviatoric stress tensor are denoted by ρ , u , P , and τ , respectively. The displacement and the time are denoted by \mathbf{x} and t , respectively. The subscripts are defined according to the Einstein summation convention. By combining the time derivative in Eq. (1) and the spatial derivative in Eq. (2), Eq. (3) is obtained, where c is the speed of sound and δ_{ij} is the Kronecker delta. By separating the density variable and the pressure variable into their static properties (ρ_0 and p_0) and fluctuating properties (ρ' and p') as in Eq. (4), Lighthill's equation in Eq. (5) is derived, where T_{ij} is the Lighthill turbulence stress tensor.

$$\frac{\partial \rho}{\partial t} + \frac{\partial \rho u_j}{\partial x_j} = 0 \rightarrow \frac{\partial^2 \rho}{\partial t^2} + \frac{\partial^2 \rho u_j}{\partial t \partial x_j} = 0 \quad (1)$$

$$\frac{\partial \rho u_i}{\partial t} + \frac{\partial \rho u_i u_j}{\partial x_j} = -\frac{\partial P}{\partial x_i} + \frac{\partial \tau_{ij}}{\partial x_j} \rightarrow \frac{\partial^2 \rho u_i}{\partial x_i \partial t} + \frac{\partial^2 \rho u_i u_j}{\partial x_i \partial x_j} = -\frac{\partial^2 P}{\partial x_i^2} + \frac{\partial^2 \tau_{ij}}{\partial x_i \partial x_j} \quad (2)$$

$$\frac{\partial^2 \rho}{\partial t^2} = \frac{\partial^2 \rho u_i u_j}{\partial x_i \partial x_j} + \frac{\partial^2 P}{\partial x_i^2} - \frac{\partial^2 \tau_{ij}}{\partial x_i \partial x_j} \rightarrow \frac{\partial^2 \rho}{\partial t^2} - c^2 \frac{\partial^2 \rho}{\partial x_i^2} = \frac{\partial^2}{\partial x_i \partial x_j} (\rho u_i u_j + (P - c^2 \rho) \delta_{ij} - \tau_{ij}) \quad (3)$$

$$\rho = \rho_0 + \rho', \quad P = p_0 + p' \quad (4)$$

$$\frac{\partial^2 \rho'}{\partial t^2} - c^2 \frac{\partial^2 \rho'}{\partial x_i^2} = \frac{\partial^2 T_{ij}}{\partial x_i \partial x_j}, \quad T_{ij} = \rho u_i u_j + (p' - c^2 \rho') \delta_{ij} - \tau_{ij} \quad (5)$$

As a governing equation of this study, the modified form of Lighthill's equation is formulated as follows. Lighthill's equation in Eq. (5) is expressed by the acoustic pressure p' as in Eq. (6) using the equation of state for isentropic flow. The Lighthill turbulence stress tensor is then reduced to $\rho u_i u_j$ (the viscous stress τ_{ij} is neglected). To solve Lighthill's equation in the frequency domain, a harmonic form of Lighthill's equation is defined as Eq. (7), where ω is the angular frequency, and p is the acoustic pressure depending on the space. In addition, both sides of Eq. (7) are divided by the media density ρ in terms of numerical analysis. The unknown acoustic pressure p on the left side of Eq. (7) represents the sound wave propagation, and the right side of the equation represents the sound source calculated from turbulent flow. The sound source term on the right side is calculated for a component oscillating at a specific frequency.

$$\frac{1}{c^2} \frac{\partial^2 p'}{\partial t^2} - \frac{\partial^2 p'}{\partial x_i^2} = \frac{\partial^2 T_{ij}}{\partial x_i \partial x_j}, \quad T_{ij} = \rho u_i u_j \quad \because \rho' = \frac{1}{c^2} p', \quad (\text{isentropic flow}) \quad (6)$$

$$\frac{\omega^2}{\rho c^2} p + \frac{1}{\rho} \frac{\partial^2 p}{\partial x_i^2} = -\frac{1}{\rho} \frac{\partial^2 T_{ij}}{\partial x_i \partial x_j} \quad \because p'(\mathbf{x}, t) = p(\mathbf{x}) \exp(i\omega t) \quad (7)$$

To perform the finite element analysis, the weak formulation of Lighthill's equation is expressed as Eq. (8) through the product rule and Green's integral theorem. The virtual acoustic pressure \tilde{p} is defined in the analysis domain Ω . In Eq. (8), n_i is the component of the outward unit normal vector \vec{n} at the boundary Γ of the analysis domain Ω . Fig. 2 shows the semicircular analysis domain for the simulation of radiated sound waves. The analysis domain is formed by square elements. The direction of outgoing waves at the outer boundary is assumed to be same as the radial direction \vec{r} from the center of semicircle. Eq. (9) is the Sommerfeld boundary condition applied at the outer boundary toward the radial direction \vec{r} . From the Sommerfeld boundary condition, the derivative of the acoustic pressure in the outward normal direction \vec{n} of the outer boundary is derived as Eq. (10), where α_θ is the parameter dependent on the angular position θ of \vec{r} . Eq. (11) is the hard wall boundary condition applied at the bottom boundary, where the derivative of the acoustic pressure in the outward normal direction \vec{n} is set to zero. The weak formulation after applying the boundary condition is described as Eq. (12), where Γ_{out} represents the outer boundary related to the outgoing sound waves.

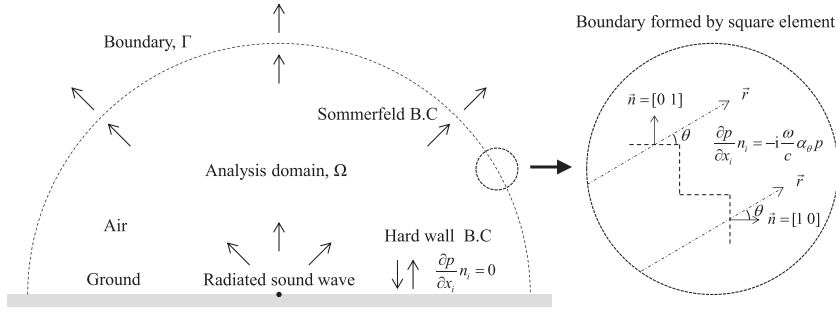


Fig. 2. Acoustic boundary conditions of the semicircular analysis domain consisting of square elements.

$$\frac{\omega^2}{\rho c^2} \int \tilde{p} p d\Omega - \frac{1}{\rho} \int \frac{\partial \tilde{p}}{\partial x_i} \frac{\partial p}{\partial x_i} d\Omega + \frac{1}{\rho} \int \tilde{p} \frac{\partial p}{\partial x_i} n_i d\Gamma = - \int \tilde{p} \frac{1}{\rho} \frac{\partial^2 T_{ij}}{\partial x_i \partial x_j} d\Omega \quad (8)$$

$$\frac{\partial p}{\partial r} = -i \frac{\omega}{c} p \quad (\text{Sommerfeld B.C.}) \quad (9)$$

$$\frac{\partial p}{\partial x_i} n_i = -i \frac{\omega}{c} \alpha_\theta p, \quad \alpha_\theta = \cos \theta \times n_1 + \sin \theta \times n_2 \quad \because \frac{\partial p}{\partial x_i} n_i = \left(\frac{\partial p}{\partial r} \cos \theta \right) n_1 + \left(\frac{\partial p}{\partial r} \sin \theta \right) n_2 \quad (10)$$

$$\frac{\partial p}{\partial x_i} n_i = 0 \quad (\text{hard wall B.C.}) \quad (11)$$

$$\frac{\omega^2}{\rho c^2} \int \tilde{p} p d\Omega - \frac{1}{\rho} \int \frac{\partial \tilde{p}}{\partial x_i} \frac{\partial p}{\partial x_i} d\Omega - i \frac{\omega}{\rho c} \alpha_\theta \int \tilde{p} p d\Gamma_{\text{out}} = - \int \tilde{p} \frac{1}{\rho} \frac{\partial^2 T_{ij}}{\partial x_i \partial x_j} d\Omega \quad (12)$$

Through the general procedure of the finite element method, the matrix equation for a local element can be expressed as Eq. (13). The bulk modulus B and the characteristic impedance z are defined as Eq. (14). In Eq. (15), the mass matrix $[M]$ and the stiffness matrix $[K]$ are defined by the linear shape function $[N]$ and the differentiated shape function $[B_i]$, respectively. The matrix $[M_{bc}]$ is related to the outer boundary Γ_{out} , and the vector $\{f_t\}$ is the aeroacoustic sound source term. The vector $\{p\}$ represents the unknown values of the acoustic pressure at the nodes of a local element. The matrix equation for the entire analysis domain is then constructed as Eq. (16). The global matrices are defined as in Eq. (17), where the notation $\langle \rangle_A$ represents the assembly of local matrices in the physical domains such as air domain, rigid domain, design domain, and sound source domain. The material properties in the air domain and the rigid domain are given in Table 1. The subscript a and r represent air and a rigid material, respectively. The density and the bulk modulus of a rigid material are set very large to implement the untransmitted sound wave [9]. The material properties in the design domain are denoted by the subscript e .

$$\left[\frac{\omega^2}{B} [M] - \frac{1}{\rho} [K] - i \frac{\omega}{z} \alpha_\theta [M_{bc}] \right] \{p\} = \{f_t\} \quad (13)$$

$$B = \rho c^2, \quad z = \rho c \quad (14)$$

$$[M] = \int [N]^T [N] d\Omega, \quad [K] = \int [B_i]^T [B_i] d\Omega, \quad [M_{bc}] = \int [N]^T [N] d\Gamma_{\text{out}}, \quad \{f_t\} = - \int [N]^T \frac{1}{\rho} \frac{\partial^2 T_{ij}}{\partial x_i \partial x_j} d\Omega \quad (15)$$

$$[\omega^2 \mathbf{M} - \mathbf{K} - i \omega \mathbf{M}_{bc}] \mathbf{p} = \mathbf{f}_t \quad (16)$$

Table 1
Material properties of air and a rigid material.

| | Density | Speed of sound | Bulk modulus | Characteristic impedance |
|--------------|-----------------------------------|------------------------------|----------------------|--------------------------|
| Air domain | $\rho_a = 1.25 \text{ kg m}^{-3}$ | $c_a = 343 \text{ m s}^{-1}$ | $B_a = \rho_a c_a^2$ | $z_a = \rho_a c_a$ |
| Rigid domain | $\rho_r = \rho_a \times 10^7$ | $c_r = c_a \times 10$ | $B_r = \rho_r c_r^2$ | $z_r = \rho_r c_r$ |

$$\begin{aligned}\mathbf{M} &= \langle \frac{1}{B_a} [M] \rangle_{A, \text{ air}} + \langle \frac{1}{B_r} [M] \rangle_{A, \text{ rigid}} + \langle \frac{1}{B_e} [M] \rangle_{A, \text{ design}}, & \mathbf{M}_{bc} &= \langle \frac{\alpha_\theta}{Z_a} [M_{bc}] \rangle_{A, \text{ outer boundary}} \\ \mathbf{K} &= \langle \frac{1}{\rho_a} [K] \rangle_{A, \text{ air}} + \langle \frac{1}{\rho_r} [K] \rangle_{A, \text{ rigid}} + \langle \frac{1}{\rho_e} [K] \rangle_{A, \text{ design}}, & \mathbf{p} &= \langle \{p\} \rangle_A, & \mathbf{f}_t &= \langle \{f_t\} \rangle_{A, \text{ source}}\end{aligned}\quad (17)$$

With regard to including the rigid domain in the finite element analysis to take into account a structure of rigid materials, related physical assumptions are explained as follows. Basically, this study deals with rigid structures that do not vibrate. In acoustic analysis including rigid structures with non-vibration, it is common to apply the hard wall boundary condition to the boundaries between rigid structures and surrounding air. However, in order to perform the topology optimization of rigid structures, the rigid domain and the design domain corresponding to the rigid structures are included in the analysis domain instead of being excluded from the analysis domain by hard wall boundaries. In this case, the material properties (the density and the bulk modulus) applied to the domain for rigid structures are adjusted so that the analysis results are almost identical to those by application of the hard wall boundary condition. Thus, unlike the acoustic-structure interaction problem, physical interactions between air and structures and the shear modulus of structures are not addressed in this study. Although some elements in the design domain can be represented as materials of intermediate state between air and a rigid material during the optimization process, the possibility of vibration by the materials of intermediate state can be ignored as long as the final result of topology optimization consists only of air and rigid materials.

2.2. Method for calculating aeroacoustic sound sources

The sound source term $\{f_t\}$ in Eq. (15) is calculated in advance to compute the finite element solution of Lighthill's equation. The sound source value that makes up $\{f_t\}$ is formulated by the flow velocity u_i as Eq. (18). Note that a component of the sound source value oscillating at a specific frequency is calculated to perform a harmonic analysis. The flow velocity u_i is divided into the mean flow velocity (time-averaged flow velocity) U_i and the fluctuating flow velocity u_i^t as Eq. (19). The mean flow velocity field $U_i(\mathbf{x})$ is obtained by the finite element analysis of the incompressible stationary RANS equations with the $k-\varepsilon$ turbulence model. The fluctuating flow velocity field $u_i^t(\mathbf{x})$ is generated by the SNGR method [23,32–39] from the preceding RANS analysis result.

$$\frac{1}{\rho} \frac{\partial^2 T_{ij}}{\partial x_i \partial x_j} \approx \frac{\partial^2 u_i u_j}{\partial x_i \partial x_j} = \frac{\partial^2 u_i}{\partial x_i \partial x_j} u_j + \frac{\partial u_i}{\partial x_j} \frac{\partial u_j}{\partial x_i} + \frac{\partial u_i}{\partial x_i} \frac{\partial u_j}{\partial x_j} + u_i \frac{\partial^2 u_j}{\partial x_i \partial x_j} \quad \because T_{ij} = \rho u_i u_j \quad (18)$$

$$u_i = U_i + u_i^t \quad (19)$$

The RANS equations are the time-averaged equations of the original Navier–Stokes equations. The momentum and mass conservation equations of the RANS equations are expressed as Eqs. (20) and (21), where U_i is the time-averaged flow velocity, and \bar{P} is the time-averaged pressure. The transport equations of the $k-\varepsilon$ turbulence model are expressed as Eqs. (22) and (23), where k is the turbulent kinetic energy and ε is the dissipation rate. The constant values of the $k-\varepsilon$ model are defined as Eq. (24) [22]. In the RANS equations, the turbulent eddy viscosity ν_t is added to the kinematic viscosity ν . The turbulent eddy viscosity ν_t is determined by the turbulent kinetic energy k and the dissipation rate ε of the transport equations. In other words, the RANS equations and the transport equations are coupled through the turbulent eddy viscosity ν_t .

$$U_j \frac{\partial U_i}{\partial x_j} + \frac{1}{\rho} \frac{\partial \bar{P}}{\partial x_i} - \frac{\partial}{\partial x_j} \left\{ (\nu + \nu_t) \left(\frac{\partial U_i}{\partial x_j} + \frac{\partial U_j}{\partial x_i} \right) \right\} = 0 \quad \nu_t = C_\mu \frac{k^2}{\varepsilon} \quad (20)$$

$$\frac{\partial U_j}{\partial x_j} = 0 \quad (21)$$

$$U_j \frac{\partial k}{\partial x_j} - \frac{\partial}{\partial x_j} \left\{ \left(\nu + \frac{\nu_t}{\sigma_k} \right) \frac{\partial k}{\partial x_j} \right\} - \nu_t \left(\frac{\partial U_i}{\partial x_j} + \frac{\partial U_j}{\partial x_i} \right) \frac{\partial U_i}{\partial x_j} + \varepsilon = 0 \quad (22)$$

$$U_j \frac{\partial \varepsilon}{\partial x_j} - \frac{\partial}{\partial x_j} \left\{ \left(\nu + \frac{\nu_t}{\sigma_\varepsilon} \right) \frac{\partial \varepsilon}{\partial x_j} \right\} - C_1 \nu_t \frac{\varepsilon}{k} \left(\frac{\partial U_i}{\partial x_j} + \frac{\partial U_j}{\partial x_i} \right) \frac{\partial U_i}{\partial x_j} + C_2 \frac{\varepsilon^2}{k} = 0 \quad (23)$$

$$C_\mu = 0.09, \quad C_1 = 1.44, \quad C_2 = 1.92, \quad \sigma_k = 1, \quad \sigma_\varepsilon = 1.3, \quad \nu = 1.42 \times 10^{-5} \text{ m}^2 \text{ s}^{-1} \quad (24)$$

In the SNGR method, the fluctuating velocity field expressed as a sum of Fourier modes with different wave numbers $\mathbf{k}_n^t (= |\mathbf{k}_n^t|)$ is synthesized with random characteristics as Eq. (25). The number of Fourier modes is denoted by N . The vectors

in Eq. (25) are defined in two dimensions as Eq. (26). For the n -th Fourier mode, \hat{u}_n^t represents the amplitude, and σ_n is the unit direction vector. The wave number vector, the phase, and the angular frequency are denoted by \mathbf{k}_n^t , ψ_n , and ω_n^t , respectively. The local convection velocity (mean flow velocity) vector obtained from the RANS analysis result is denoted by \mathbf{U} . The unit direction vector σ_n is determined by the random parameter θ_n as Eq. (27). From the incompressibility condition of the turbulent velocity field, the wave number vector \mathbf{k}_n^t is perpendicular to the unit direction vector σ_n . Therefore, the direction of the wave number vector is defined by the random parameter θ_n as Eq. (28). The phase ψ_n is also randomly determined in the range of $0 \leq \psi_n \leq 2\pi$ assuming the homogeneous turbulence. The angular frequency ω_n^t is defined by the turbulent kinetic energy k and the wave number k_n^t as Eq. (29) [34–36]. Then, the angular frequency ω_n that reflects the convection effect of mean flow is defined. The angular frequency ω_n is used to extract the Fourier modes that contribute to the sound source value at a specific frequency.

$$\mathbf{u}^t(\mathbf{x}, t) = 2 \sum_{n=1}^N \hat{u}_n^t \sigma_n \cos\{\mathbf{k}_n^t \cdot (\mathbf{x} - t\mathbf{U}) + \psi_n + \omega_n^t t\} \quad (25)$$

$$\mathbf{u}^t = [u_1^t \ u_2^t] \quad \sigma_n = [\sigma_{1,n} \ \sigma_{2,n}] \quad \mathbf{k}_n^t = [k_{1,n}^t \ k_{2,n}^t] \quad \mathbf{x} = [x_1 \ x_2] \quad \mathbf{U} = [U_1 \ U_2] \quad (26)$$

$$\sigma_{1,n} = \cos \theta_n, \quad \sigma_{2,n} = \sin \theta_n \quad (0 \leq \theta_n \leq 2\pi) \quad (27)$$

$$k_{1,n}^t = k_n^t \cos\left(\theta_n + \frac{\pi}{2}\right), \quad k_{2,n}^t = k_n^t \sin\left(\theta_n + \frac{\pi}{2}\right) \quad (28)$$

$$\omega_n^t = k_n^t \left(\frac{2}{3}k\right)^{\frac{1}{2}} \rightarrow \omega_n = \frac{\omega_n^t - k_{1,n}^t U_1 - k_{2,n}^t U_2}{2\pi} \quad (29)$$

The amplitude \hat{u}_n^t is calculated from the Von Karman–Pao spectrum, which represents the energy spectrum $E(k^t)$ according to the wave number k^t [40]. The Von Karman–Pao spectrum is formulated as Eqs. (30) and (31). The turbulent kinetic energy k and the dissipation rate ε are obtained from the RANS analysis result. The wave number of maximum energy corresponding to the peak position in the spectrum is denoted by k_e . The Kolmogorov wave number and the turbulence length scale are denoted by k_η and Λ , respectively. The numerical constant α is determined from the relation $k = \int_0^\infty E(k^t) dk^t$, meaning that the turbulent kinetic energy is equal to the total surface area beneath the spectrum graph. The parameter f_L is a calibration factor, and ν is the kinematic viscosity. Fig. 3(a) represents an example graph of the Von Karman–Pao spectrum, which is divided into the bandwidth Δk^t . The amplitude \hat{u}_n^t corresponding to the wave number k^t of the n -th Fourier mode is calculated as Eq. (32). This equation means that the kinetic energy per unit mass for the root mean square of the fluctuating flow velocity in the n -th Fourier mode is equal to the surface area beneath the spectrum graph within the bandwidth Δk^t at the wave number k^t . In the implementation of the SNGR method, the fluctuating flow velocity field is synthesized independently in each subdomain with a size of l_{sub} as Fig. 3(b). Therefore, \hat{u}_n^t , θ_n , ψ_n , and ω_n are calculated in each subdomain using the mean flow properties (U_1 , U_2 , k , and ε) averaged in the subdomain. The fluctuating flow velocity fields in all subdomains are combined to generate the entire fluctuating flow velocity field.

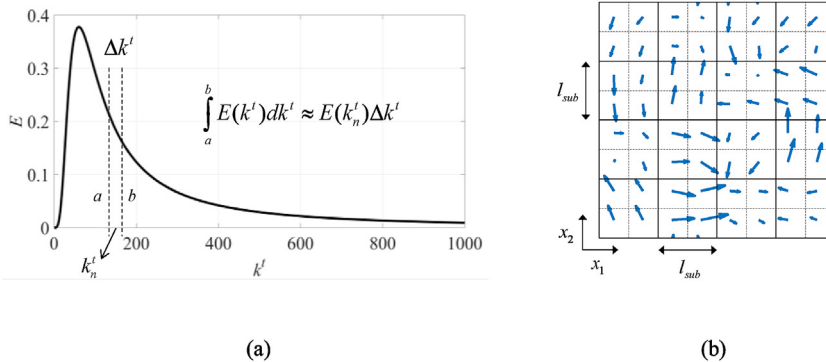


Fig. 3. Example of (a) the Von Karman–Pao spectrum and (b) the synthesized fluctuating flow velocity field.

$$E(k^t) = \alpha \frac{2k}{3k_e} \left(\frac{k^t}{k_e} \right)^4 \left[1 + \left(\frac{k^t}{k_e} \right)^2 \right]^{-17/6} \exp \left[-2 \left(\frac{k^t}{k_e} \right)^2 \right] \quad (30)$$

$$k_e = \frac{9\pi}{55} \frac{\alpha}{A}, \quad k_\eta = \nu^{-3/4} \varepsilon^{1/4}, \quad A = f_L \frac{\left(\frac{2}{3} k \right)^{3/2}}{\varepsilon}, \quad \alpha = 1.45276, \quad f_L = 1 \quad (31)$$

$$\hat{u}_n^t = \sqrt{E(k_n^t) \Delta k^t} \quad \therefore \frac{1}{2} \left(\frac{2\hat{u}_n^t}{\sqrt{2}} \right)^2 = E(k_n^t) \Delta k^t \quad (32)$$

2.3. Aeroacoustic analysis results by random aeroacoustic sound sources

In this subsection, aeroacoustic analysis results using Lighthill's equation are presented according to the method described earlier. The presented analysis conditions are applied to the optimization problems in the following sections. Fig. 4 shows the semicircular analysis domain with the radius R of 6 m. At the center of the semicircular analysis domain, an aeroacoustic sound source region is positioned. The bottom boundary of the analysis domain is modeled with the sound reflection condition (hard wall), and the outer boundary is modeled with the sound non-reflection condition (Sommerfeld boundary condition). The analysis domain is discretized by four-node square elements of which size is 0.01 m by 0.01 m.

To generate aeroacoustic sound sources applied to the analysis domain of Fig. 4, a mean flow analysis by the RANS equation and the k - ε turbulence model is conducted using the finite element analysis software (COMSOL). The flow analysis domain is shown in Fig. 5 with boundary conditions. Taking into account the flow injected with a velocity of 30 m s^{-1} , the Dirichlet boundary condition is imposed on the left side of the flow analysis domain. The bottom side is set to the ground (hard wall). The Neumann boundary condition is imposed on the top and the right side. Fig. 6 shows the visualized mean flow properties.

In the synthesis of the fluctuating flow velocity field based on the SNGR method, the size of subdomains is set to 0.02 m, and the range of the wave number k_n^t for Fourier modes is set from 0.5 rad m^{-1} to 299.5 rad m^{-1} with intervals of 1 rad m^{-1} . It is assumed that the kinetic energy of the Fourier modes with a larger wave number is negligible. Then, the sound source values of Lighthill's equation are calculated from the flow velocity, which is represented by sum of the mean flow velocity and

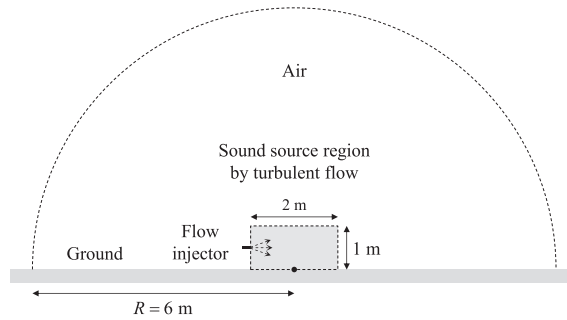


Fig. 4. Acoustic analysis domain including the aeroacoustic sound source region.

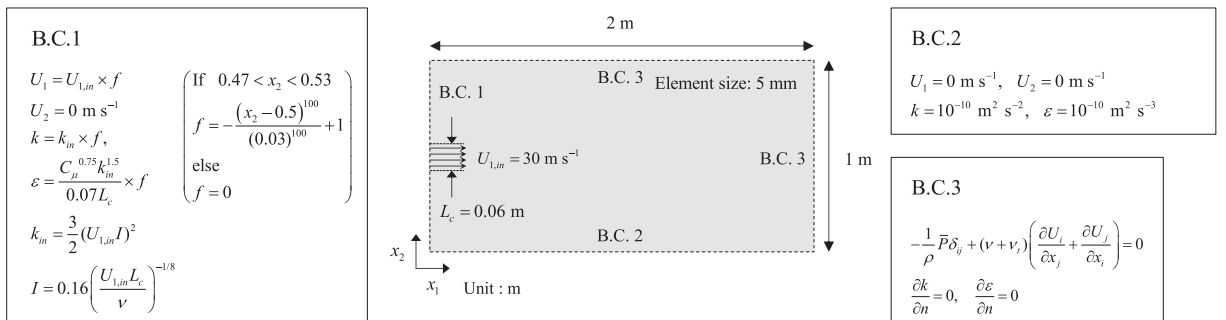


Fig. 5. Flow analysis domain and applied boundary conditions.

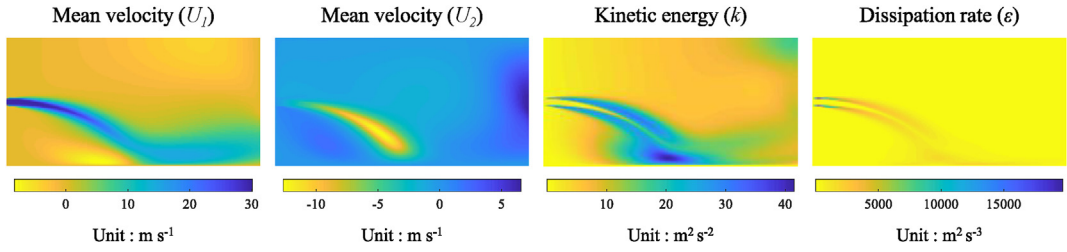


Fig. 6. Mean flow analysis results by the RANS equations and the $k-\epsilon$ turbulence model.

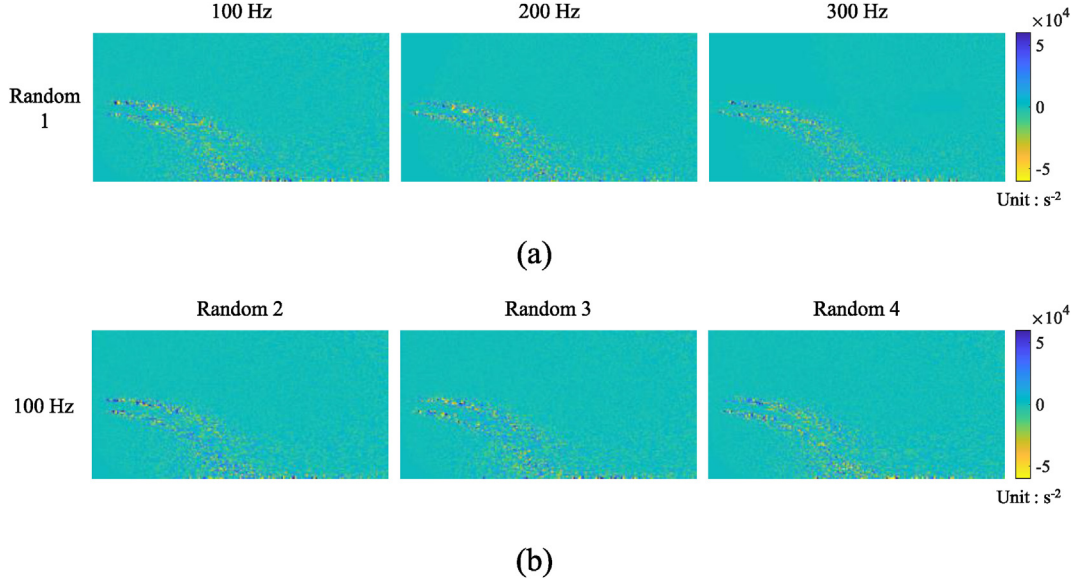


Fig. 7. Visualized sound source values of Lighthill's equation (a) for the different frequencies and (b) for the different random conditions.

the fluctuating flow velocity. A continuous frequency range is divided into the intervals of 1 Hz to generate an aeroacoustic sound source at a specific frequency. Fig. 7(a) shows the visualized sound source values calculated by Eq. (18) for the frequencies of 100 Hz, 200 Hz, and 300 Hz. Since an aeroacoustic sound source is generated through the randomly determined parameters, different aeroacoustic sound sources are taken into account as Fig. 7(b). The distributions of the acoustic pressure and the sound pressure level for the generated aeroacoustic sound sources are shown in Figs. 8 and 9, respectively. The sound pressure level SPL is defined as Eq. (33), where p_{ref} is the reference acoustic pressure.

$$\text{SPL} = 10 \log \frac{|p|^2}{|p_{ref}|^2}, \quad p_{ref} = 2 \times 10^{-5} \text{ Pa} \quad (33)$$

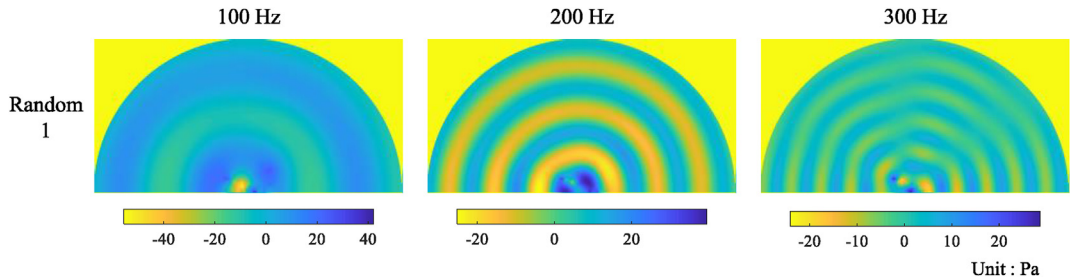


Fig. 8. Distributions of the acoustic pressure for the different frequencies.

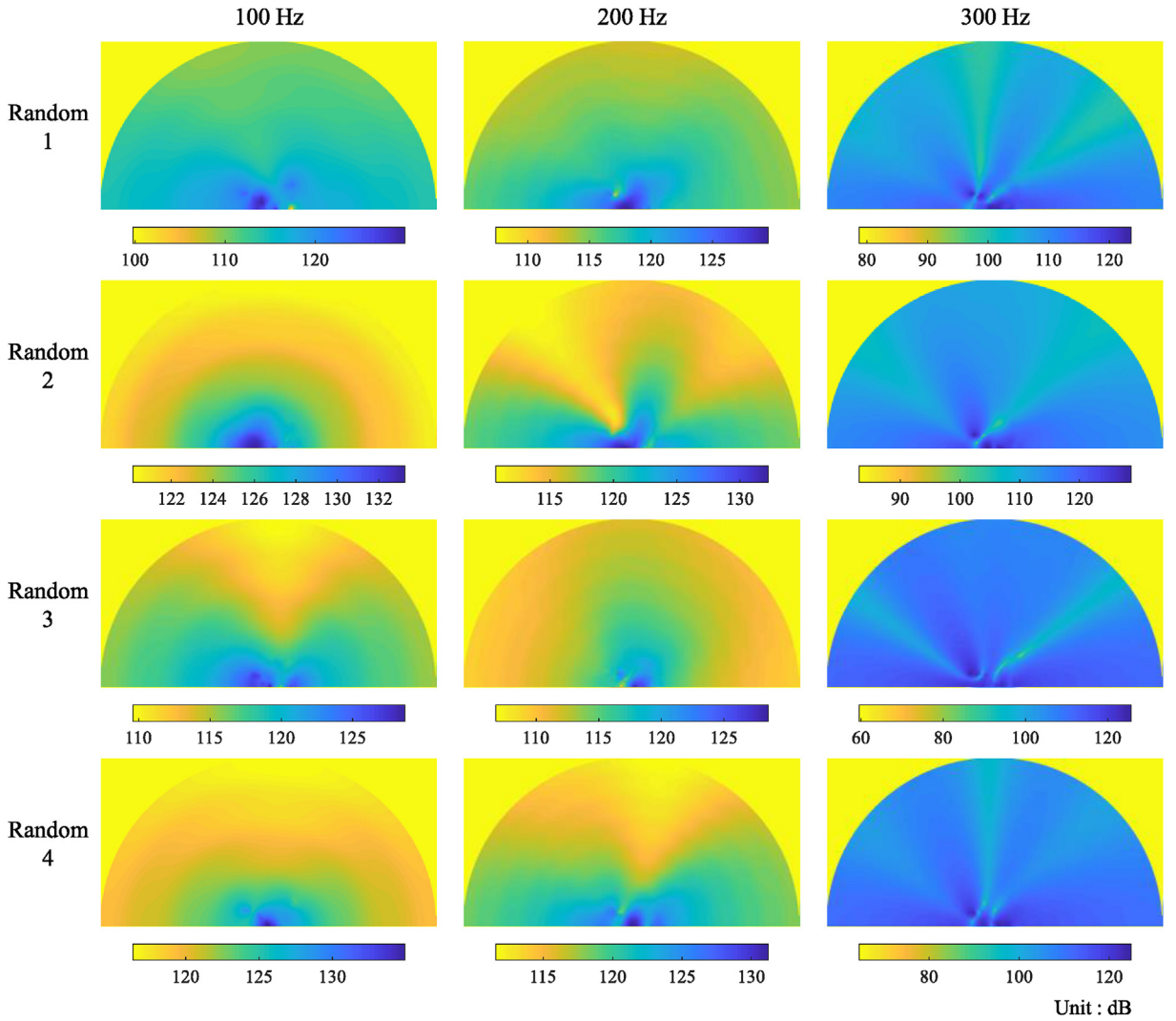


Fig. 9. Distributions of the sound pressure level for the different aeroacoustic sound sources.

3. Definition of a topology optimization problem

3.1. Design problem for the top shape of noise barrier

A design problem for the top shape of noise barrier is defined taking into account a distributed aeroacoustic sound source. Fig. 10 shows the straight rigid noise barrier and the design domain at the top of the barrier. The distance D_B between the center of the analysis domain and the barrier, the barrier height H_B , and the barrier thickness t_B are represented in Fig. 10. The top shape is designed by a material layout which is parameterized by design variables. The design variables are optimized to maximize the insertion loss at the sound measurement area. The position of the sound measurement area is established to reduce the noise heard by someone who exists behind the barrier.

3.2. Representation of material layout by design variables

A continuous design variable between 0 and 1 is assigned to each finite element in the design domain to represent a material layout. For the material properties of the e -th element in the design domain, the inverse of the density ρ_e and the inverse of the bulk modulus B_e are linearly interpolated by the function $\varphi_e(\gamma)$ as Eq. (34) [41], where the vector γ represents the design variables. The function φ_e is called the TO density (the conventionally defined density in topology optimization) in this study. When the TO density φ_e is 0, the material state is air. On the contrary, the material state is a rigid material when the TO density φ_e is 1. When the TO density φ_e is not fully convergent to 0 or 1, the element is an intermediate material state

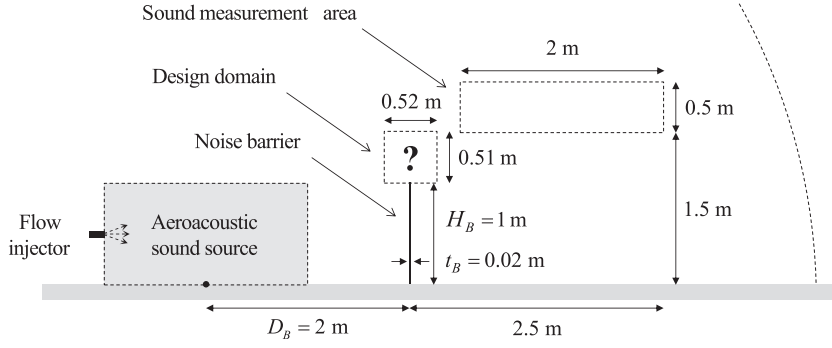


Fig. 10. Design domain and sound measurement area for the design of noise barrier.

between air and the rigid material. This kind of element is called a gray element. The TO density φ_e should be appropriately defined so that optimized material layouts do not include many of these gray elements [18,19].

$$\frac{1}{\rho_e} = \frac{1}{\rho_a} + \left(\frac{1}{\rho_r} - \frac{1}{\rho_a} \right) \times \varphi_e(\gamma), \quad \frac{1}{B_e} = \frac{1}{B_a} + \left(\frac{1}{B_r} - \frac{1}{B_a} \right) \times \varphi_e(\gamma), \quad \gamma = [\gamma_1 \ \gamma_2 \ \cdots \ \gamma_e \ \cdots] \quad (34)$$

The TO density φ_e in this study is defined by the linear filter and the sigmoid function [29]. The original design variable γ_e at the e -th element is converted to the filtered value d_e by the design variables of neighboring elements as Eq. (35) [17,18]. The weight factor w_{ej} of a neighboring element is defined by Eq. (36). The index set N_e for the neighboring elements within the filter radius \bar{R} is determined by the distance $\bar{d}(e, j)$ between the e -th and j -th elements. The filtered value d_e is then applied to the sigmoid function of Eq. (37) to obtain the TO density φ_e . Fig. 11 shows the sigmoid function depending on the sigmoid parameter s .

$$d_e = \sum_j w_{ej} \gamma_j \quad (35)$$

$$w_{ej} = \begin{cases} \frac{\bar{R} - \bar{d}(e, j)}{\sum_{k \in N_e} \bar{R} - \bar{d}(e, k)} & j \in N_e \\ 0 & j \notin N_e \end{cases} \quad N_e = \{j : \bar{d}(e, j) \leq \bar{R}\} \quad (36)$$

$$\varphi_e = [1 + \exp(-s(d_e - 0.5))]^{-1} \quad (37)$$

3.3. Formulation of optimization problem

The optimization problem is formulated as Eq. (38) for the design problem described in section 3.1. The objective function $f_{obj}(\gamma)$ is defined as the minus of the insertion loss IL as Eq. (39). The insertion loss means the decreased noise level resulting from the insertion of a certain rigid structure in the air media. The insertion loss IL is calculated from the complex acoustic

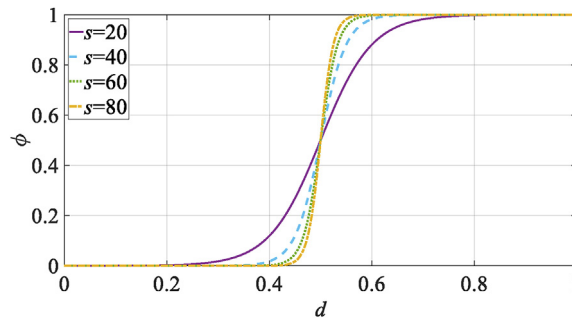
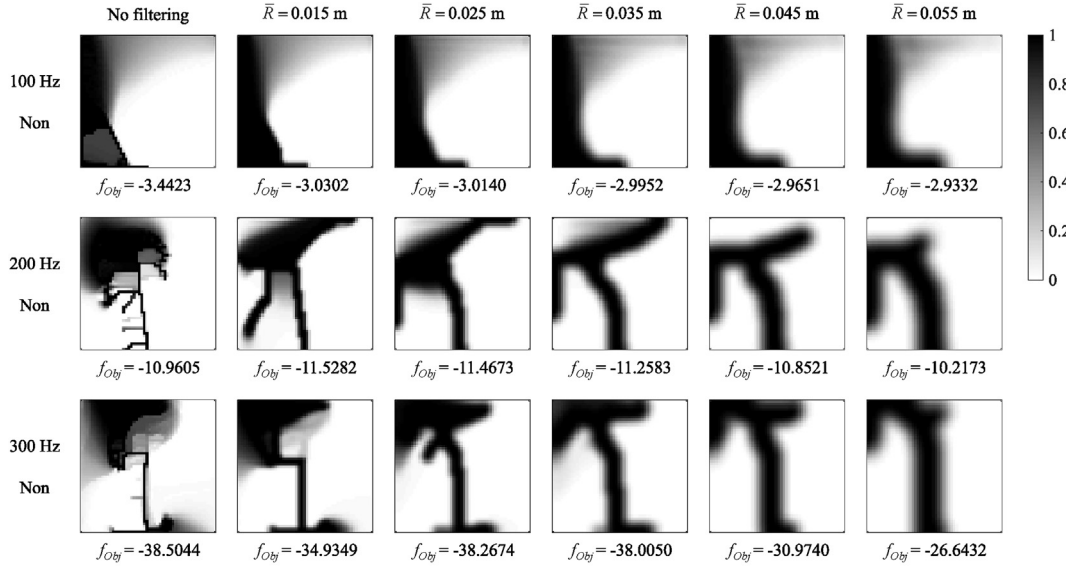
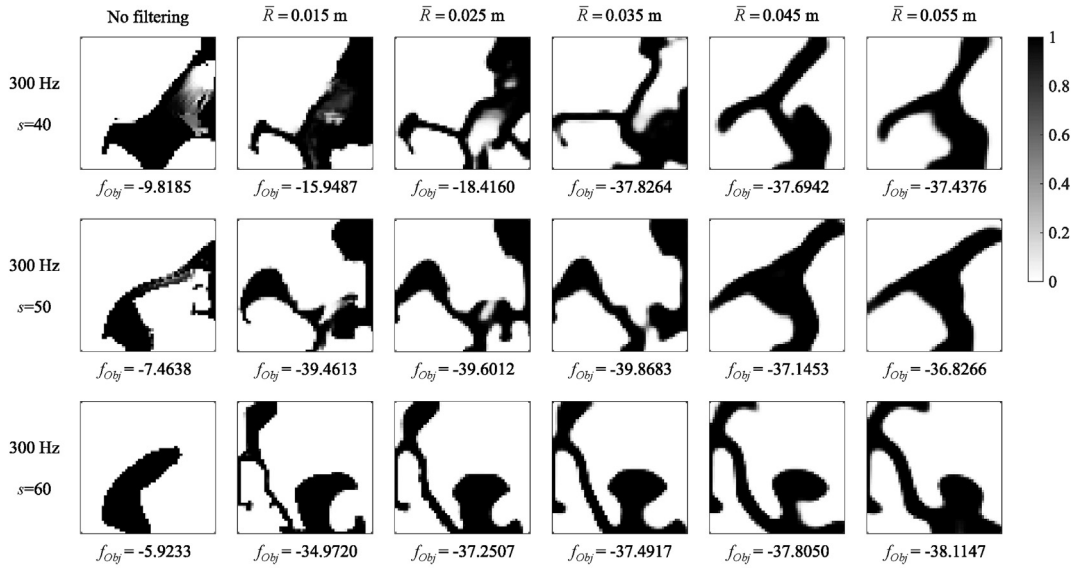


Fig. 11. Sigmoid functions with the sigmoid parameter s .

pressure p_i which is measured at the nodal points in the sound measurement area. The acoustic pressure denoted by \hat{p}_i is the measured value when there are no rigid structures in the design domain. The minus sign is imposed to maximize the insertion loss IL through the optimization algorithm that minimizes the objective function. The constraint parameter β_{rigid} is specified to limit material usage. The notation NE is the number of elements in the design domain. The formulated optimization



(a)



(b)

Fig. 12. Effect of the filter radius on the optimized material layout. (a) Results when the sigmoid penalty function is not applied in the interpolation method and (b) results when the sigmoid penalty function is applied in the interpolation method.

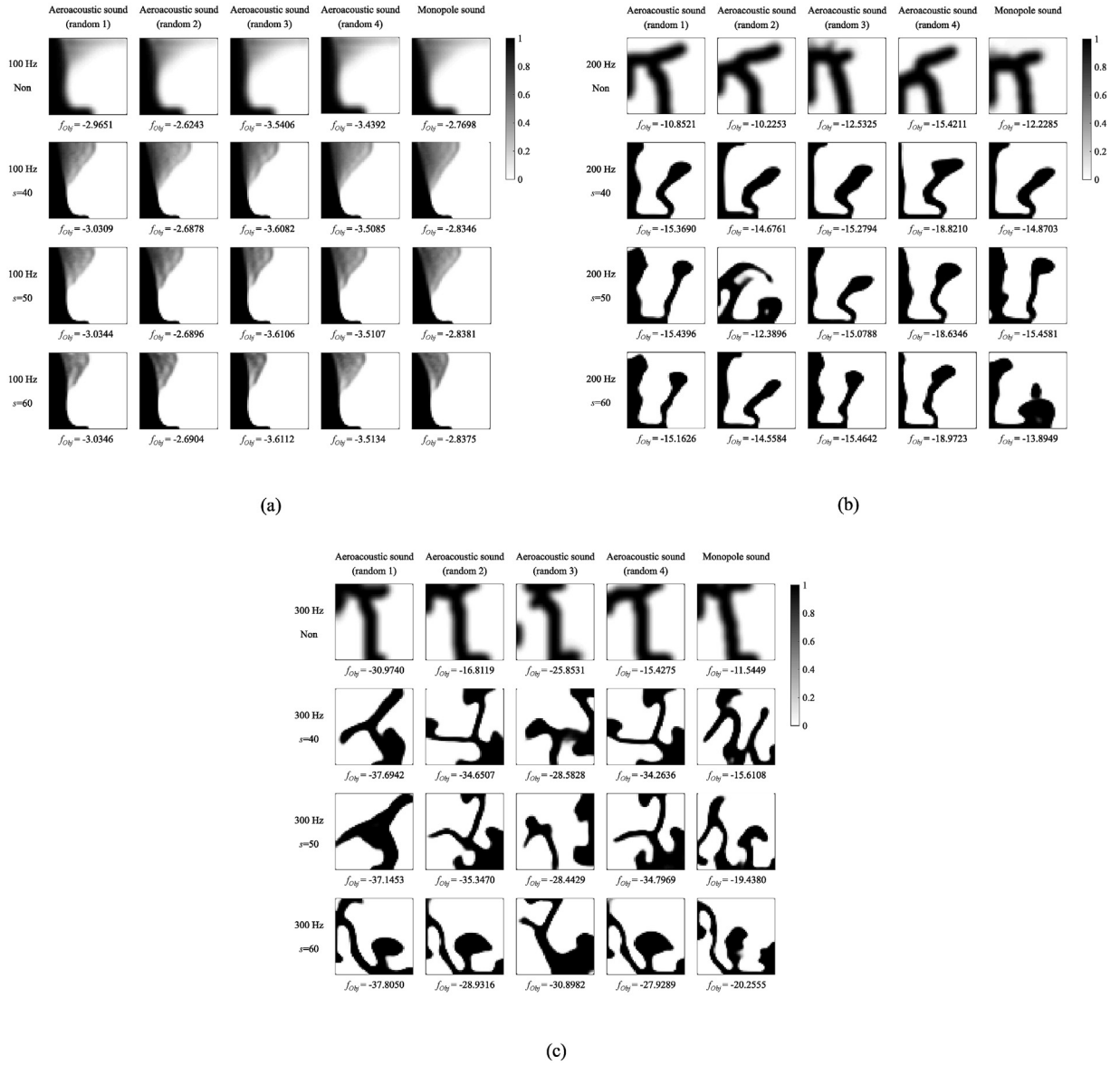


Fig. 13. Optimized material layouts for the different conditions of sound source, performed at three single frequencies. (a) 100 Hz, (b) 200 Hz, and (c) 300 Hz.

problem is solved through the MMA algorithm [30], which uses the gradients of the objective function to update the design variables.

$$\begin{aligned}
 &\text{Minimize } f_{obj}(\gamma) \quad \gamma = [\gamma_1, \dots, \gamma_{NE}], \quad 0 \leq \gamma_e \leq 1 \\
 &\text{Subject to } \sum_{e=1}^{NE} \gamma_e / NE - \beta_{\text{rigid}} \leq 0
 \end{aligned} \tag{38}$$

Table 2

Insertion loss of the straight barrier depending on the material properties determined by the TO density φ_e .

| | | | | | | | | |
|-------------|--------------------|--------------------|--------------------|--------------------|--------------------|--------------------|--------------------|-----------------------|
| φ_e | 0 | 0.5 | 0.9 | 0.95 | 0.98 | 0.99 | 0.999 | 1 |
| ρ_e | 1.25 | 2.50 | 1.25×10^1 | 2.50×10^1 | 6.25×10^1 | 1.25×10^2 | 1.25×10^3 | 1.25×10^7 |
| B_e | 1.47×10^5 | 2.94×10^5 | 1.47×10^6 | 2.94×10^6 | 7.35×10^6 | 1.47×10^7 | 1.47×10^8 | 1.47×10^{14} |
| IL (dB) | 0 | -0.01 | 0.23 | 0.81 | 2.19 | 3.13 | 3.99 | 4.06 |

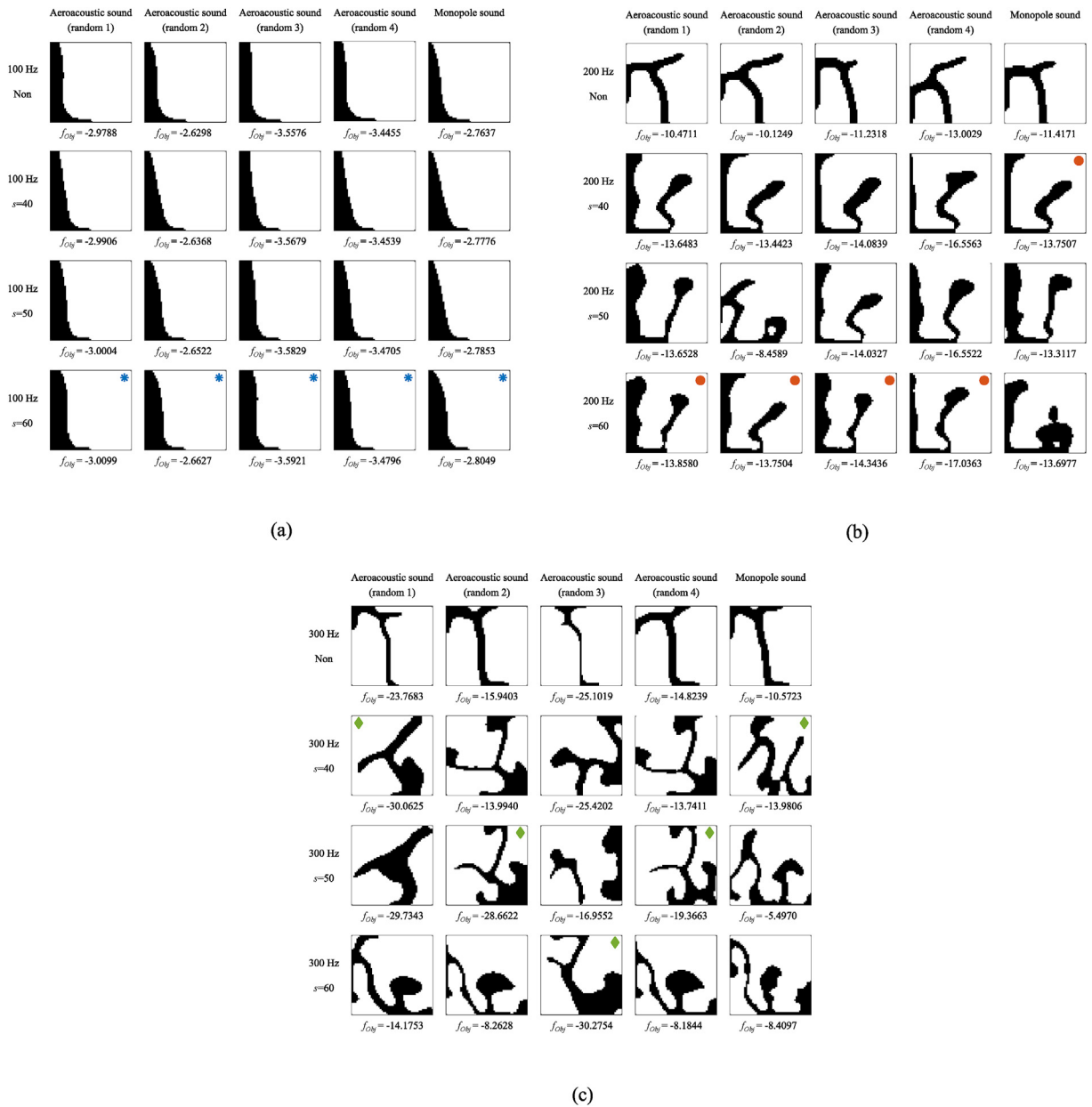


Fig. 14. Postprocessed layouts of the optimized material layouts for the different conditions of sound source, performed at three single frequencies. (a) 100 Hz, (b) 200 Hz, and (c) 300 Hz.

$$f_{Obj} = -IL = 10 \log \left(\frac{|p_1|^2 + |p_2|^2 + \dots}{|\hat{p}_1|^2 + |\hat{p}_2|^2 + \dots} \right) \quad (39)$$

The gradients of the objective function with respect to the design variables are formulated using the adjoint variable method as Eq. (40). The operators Re and conj denote the real number and the complex conjugate, respectively. The row vector \mathbf{L}_i and the matrix \mathbf{S} are defined as Eq. (41). The row vector \mathbf{L}_i has an element of which value is 1 with the other elements of which values are 0 (for example, $[0 \ 0 \ 0 \ \dots \ 1 \ \dots \ 0 \ 0 \ 0]$). The element of “value 1” corresponds to the nodal point for measurement. The matrix \mathbf{S} indicates the matrix on the left-hand side of Eq. (16)

$$-\frac{\partial IL}{\partial \gamma} = 2\text{Re} \left[10 \frac{(\text{conj}(p_1)\mathbf{L}_1 + \text{conj}(p_2)\mathbf{L}_2 + \dots)}{(p_1 \text{conj}(p_1) + p_2 \text{conj}(p_2) + \dots) \ln 10} \frac{\partial \mathbf{p}}{\partial \gamma} \right], \quad \frac{\partial \mathbf{p}}{\partial \gamma} = -\mathbf{S}^{-1} \frac{\partial \mathbf{S}}{\partial \gamma} \mathbf{p} \quad (40)$$






$$p_i = \mathbf{L}_i \mathbf{p}, \quad \mathbf{S} = \omega^2 \mathbf{M} - \mathbf{K} - i\omega \mathbf{M}_{bc} \quad (41)$$

When taking into account the insertion losses at multiple target frequencies, the objective function is defined as Eq. (42). The subscript MF denotes the combination of multiple frequencies, and the subscript F_i denotes each single frequency. The weight factor α_i of each frequency is set to $1/N_F$, where N_F denotes the number of multiple frequencies. The gradients of the objective function are formulated as Eq. (43).

$$f_{Obj} = -IL_{MF} = \alpha_1 \left(10 \log \frac{|p_1|^2 + |p_2|^2 + \dots}{|\hat{p}_1|^2 + |\hat{p}_2|^2 + \dots} \right)_{F_1} + \alpha_2 \left(10 \log \frac{|p_1|^2 + |p_2|^2 + \dots}{|\hat{p}_1|^2 + |\hat{p}_2|^2 + \dots} \right)_{F_2} + \dots \quad (42)$$

$$-\frac{\partial IL_{MF}}{\partial \gamma} = 2\text{Re} \left[\alpha_1 \left\{ 10 \frac{(\text{conj}(p_1)\mathbf{L}_1 + \text{conj}(p_2)\mathbf{L}_2 + \dots)}{(p_1 \text{conj}(p_1) + p_2 \text{conj}(p_2) + \dots) \ln 10} \frac{\partial \mathbf{p}}{\partial \gamma} \right\}_{F_1} + \alpha_2 \left\{ 10 \frac{(\text{conj}(p_1)\mathbf{L}_1 + \text{conj}(p_2)\mathbf{L}_2 + \dots)}{(p_1 \text{conj}(p_1) + p_2 \text{conj}(p_2) + \dots) \ln 10} \frac{\partial \mathbf{p}}{\partial \gamma} \right\}_{F_2} + \dots \right] \quad (43)$$

In the optimization examples of this study, the default values for the constraint parameter β_{rigid} , the initial design variable $\gamma_{e,\text{initial}}$, and the move-limit parameter are set as follows. The value of the constraint parameter β_{rigid} in Eq. (38) is set to 0.3, which means that the materials deployed in the design domain can account for up to approximately 30%. The initial value $\gamma_{e,\text{initial}}$ of design variables is set to 0.3, which is equal to the value of the constraint parameter β_{rigid} . The move-limit parameter means a limited distance to move the design variable in the design variable space. In the use of the MMA optimization

| | | Optimum for aeroacoustic sound (random 1) | Optimum for aeroacoustic sound (random 2) | Optimum for aeroacoustic sound (random 3) | Optimum for aeroacoustic sound (random 4) | Optimum for monopole sound |
|---------------------------------|----------------------------------|---|---|---|--|---|
| | | $s=40$ | $s=50$ | $s=60$ | $s=50$ | $s=40$ |
| Best layout at 300 Hz | |  |  |  |  |  |
| IL at 300 Hz (ranking) | Aeroacoustic sound (random 1) | 30.0625 | 16.4397 | 12.9554 | 11.5895 | 20.1600 |
| | Aeroacoustic sound (random 2) | 15.9417 | 28.6622 | 10.8126 | 18.3177 | 18.7140 |
| | Aeroacoustic sound (random 3) | 12.8962 | 9.1269 | 30.2754 | 6.1434 | 11.3678 |
| | Aeroacoustic sound (random 4) | 14.4404 | 25.6711 | 10.2275 | 19.3663 | 17.1250 |
| | Average value (random 1~4) | 18.3352 (2) | 19.9750 (1) | 16.0677 (4) | 13.8542 (5) | 16.8417 (3) |
| | Monopole sound | 9.7865 (4) | 15.7659 (2) | 6.8353 (5) | 19.1528 (1) | 13.9806 (3) |

Unit : dB

Fig. 15. Comparison between the best layouts at 300 Hz, obtained for each condition of sound source.

algorithm, the move-limit parameter is gradually reduced by 0.8 times from the initial value of 0.05. If the objective function value for the updated design variables is larger than the objective function value for the current design variables, the current design variables are updated again by reducing the move-limit parameter. The iterative optimization process is interrupted when the objective function is sufficiently convergent with the variation value less than 10^{-3} dB.

4. Topology optimization results

4.1. Optimized material layouts depending on the interpolation method of material properties

Before exploring various optimization results, the preliminary optimization is performed to determine the appropriate value of the filter radius \bar{R} in the interpolation method of material properties. In the preliminary optimization, the aeroacoustic sound sources denoted by “Random 1” in Fig. 7(a) are applied, and three single frequencies of 100 Hz, 200 Hz, and 300 Hz are dealt with. Fig. 12(a) shows the optimized material layouts depending on the filter radius when the sigmoid penalty function is not applied in the interpolation method. The color of element in the optimized material layout represents the TO density φ_e . As the filter radius increases, the material layout becomes more distinct with fewer gray elements, particularly in the results for 200 Hz and 300 Hz. Fig. 12(b) shows the optimized material layouts at the frequency of 300 Hz depending on the filter radius when the sigmoid penalty function in Eq. (37) is applied in the interpolation method. The sigmoid parameter s is set to three values of 40, 50, and 60. When the sigmoid parameter s is set to 40 or 50, the material layouts obtained for the filter radius below the 0.035 m appear indistinct by some gray elements and are inappropriate in

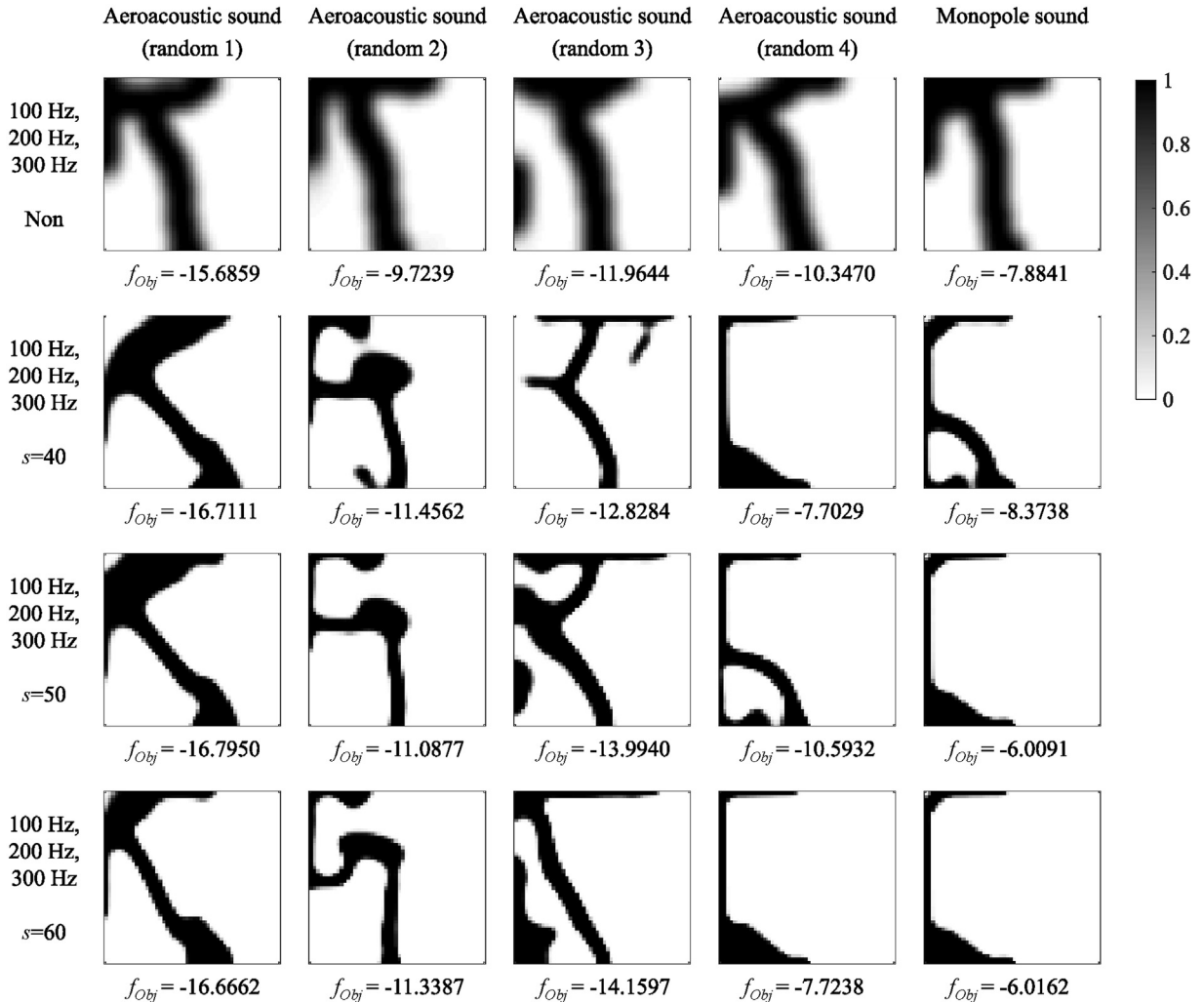


Fig. 16. Optimized material layouts for the different conditions of sound source, performed on the combination of three frequencies (100 Hz, 200 Hz, and 300 Hz).

terms of manufacture. From the results in Fig. 12, the filter radius of 0.045 m is selected as the appropriate value for further optimization.

In the results of Fig. 12(b), some readers may have doubts about the differences in the optimized material layouts with different selection of the sigmoid parameter s . For the cases that material properties are interpolated by design variables through the linear function or the sigmoid functions with different slopes, it is theoretically reasonable for the design variables to converge to the local optimum representing the same or similar design result compared with the different cases. To meet this theoretical expectation, design variables should be updated within a very small range in the optimization process and the number of updates should be very large. However, this way of updating design variables is practically difficult due to the enormous convergence time into the local optimal solution. Thus, in practice, the updates of design variables are set to an appropriate range through the adjustment of the move-limit parameter, which results in a failure to reach the theoretically exact local optimum, and a local optimum representing a different design result may be obtained. In this context, the use of the sigmoid function is effective in mitigating the problem of gray elements at the local optimum as shown in Fig. 12, but provides somewhat different design results with the different selections of the sigmoid parameter s . The results in Fig. 12(b) by the sigmoid parameter s can also be attributed to the physical system of the present study in which the sound field changes sensitively with slight changes in material distribution during the topology optimization process.

4.2. Optimized material layouts depending on the random aeroacoustic sound source

In this subsection, optimized material layouts for different random aeroacoustic sounds are studied. Optimized material layouts for the monopole sound are also presented for comparison. When the monopole sound is applied to the finite element analysis, the acoustic pressure at the center of the semicircular analysis domain is set to $1+1i$ Pa. Fig. 13 shows the optimization results performed at the three single frequencies for the different conditions of sound source. For each condition of sound source, the optimization is performed with the different conditions of interpolation method. One condition is the non-application of the sigmoid penalty function (denoted by “non” in the figures), the other conditions are the application of the sigmoid penalty function with different values of the sigmoid parameter s . In the optimization results at the frequency of 100 Hz, the optimized layouts are almost similar between the results for the different sound sources. The results also do not much differ depending on the interpolation method. While it may be possible to consider increasing the sigmoid parameter s to exceed 60 in order to reduce gray elements, this causes little reduction of the objective function value in the initial iteration stage during the optimization at the frequency of 100 Hz. This is due to the very low slope of the sigmoid function at the value of 0.3 corresponding to the initial value of design variables. In the optimization results at the frequency of 200 Hz, the optimized layouts are similar between the results for the different sound sources. However, the optimized layouts much differ depending on whether the sigmoid penalty function is applied or not. In the optimization results at the frequency of 300 Hz, the optimized layout varies under each condition although some common features are found.

Postprocessing is then performed to obtain the layout of fully rigid materials from the optimized material layout that contains gray elements. In other words, the TO density φ_e of each element is converted to 0 or 1 according to a specific criteria value φ_c . The TO density φ_e above the criteria value φ_c is converted to 1, and the TO density φ_e below the criteria value φ_c is converted to 0 as Eq. (44). To estimate an appropriate criteria value φ_c , a simple test can be performed on the straight barrier in

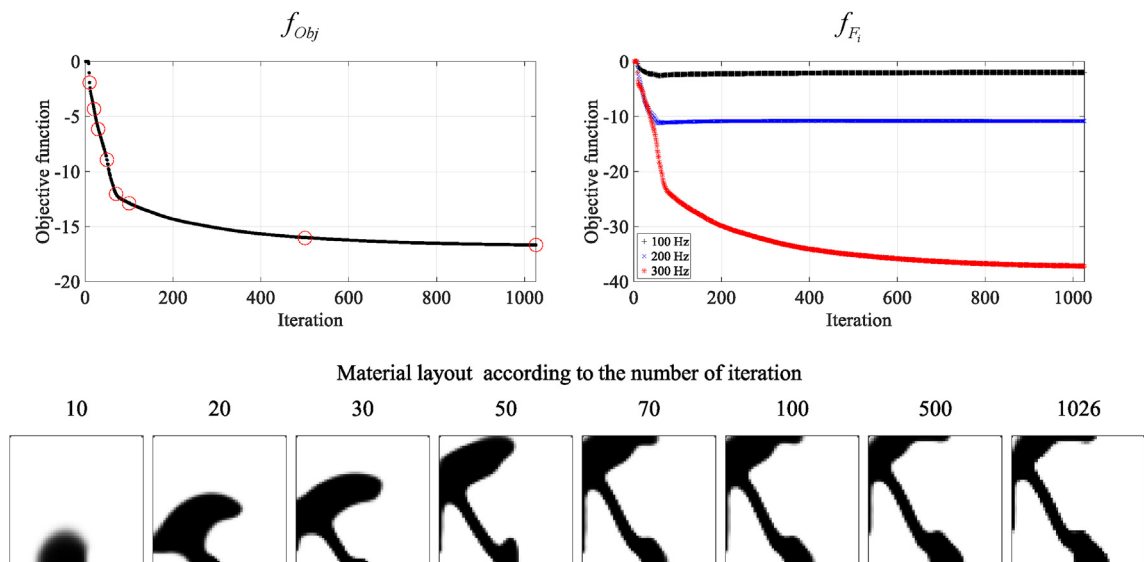


Fig. 17. Objective function graph and material layouts at the different iteration numbers.

Fig. 10 without a top structure. In this test, the insertion loss by the straight barrier is calculated depending on the material properties assigned to the straight barrier. Here, the material properties are determined by the TO density φ_e based on Eq. (34). Table 2 shows the insertion losses calculated at the frequency of 300 Hz for the monopole sound. Although not enough, the straight barrier has an effect of blocking sound waves when the TO density φ_e is greater than 0.9. From this result, the optimized material layout is converted for 10 criteria values of φ_c from 0.90 to 0.99 with intervals of 0.01. Among the 10 converted layouts, the layout with the lowest value of objective function is selected as the postprocessed layout. The reason why the conversion is performed on the multiple criteria values is that the objective function value after the conversion may vary significantly depending on the criteria value when the feature of the optimized material layout is complex. In the selection of the postprocessed layout, converted layouts with non-manufacturable features, such as a separate part, are excluded. In a few cases, some parts of the selected layout may be deleted forcibly if all of the converted layouts have non-manufacturable features.

$$\text{If } \varphi_e > \varphi_c, \quad \varphi_e = 1, \quad \text{else,} \quad \varphi_e = 0 \quad (44)$$

Fig. 14 shows the postprocessed material layouts for the optimized material layouts in Fig. 13. In the postprocessed layouts at the frequency of 100 Hz, rigid materials are distributed on the left side of the design domain to form a L-shape. This shape can effectively reflect the sound waves radiated from the sound source in the opposite direction. In the postprocessed layouts

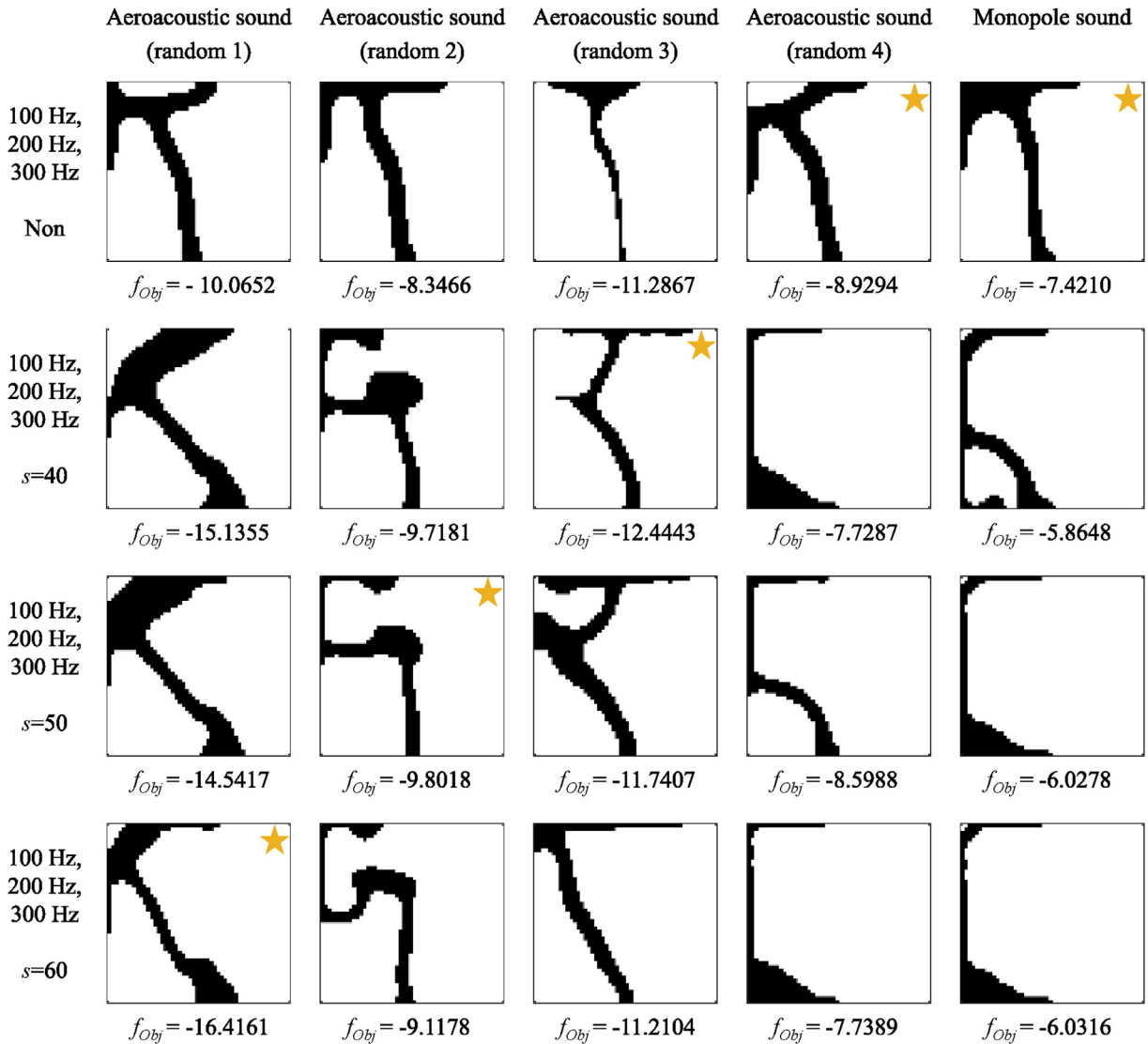


Fig. 18. Postprocessed layouts of the optimized material layouts for the different conditions of sound source, performed on the combination of three frequencies (100 Hz, 200 Hz, and 300 Hz).

at the frequency of 200 Hz, rigid materials are distributed like a left curved T-shape, when the sigmoid penalty function is not applied. The left part of this shape can interfere with the diffraction of the sound waves that faces the lower part of the shape. On the other hand, when the sigmoid penalty function is applied, rigid materials are not only distributed on the left side but toward the upper side in the rear of it. As a quarter of the wavelength at 200 Hz is 0.43 m, the cavity formed by the material distributions can cause destructive interference of sound waves. In the postprocessed layouts at the frequency of 300 Hz, rigid materials are distributed similarly to the T-shape, when the sigmoid penalty function is not applied. Compared to the T-shapes obtained at 200 Hz, the lengths of the upper parts are shorter. When the sigmoid penalty function is applied, rigid materials are distributed to form multiple cavities. These cavities are thought to cause some destructive interference of sound waves at 300 Hz. In Fig. 14, the layouts with a marker refer to the best layout with the lowest value of objective function among the layouts obtained under the same condition of sound source. In most cases, the objective function value of the postprocessed layout is higher than that of the layout before postprocessing.

In Fig. 15, the insertion losses at 300 Hz for the different random aeroacoustic sounds and the monopole sound are compared between the five best layouts at 300 Hz, obtained for each condition of sound source. Each of the three best layouts obtained for the aeroacoustic sounds (random 1–3) indicates the highest insertion loss among the five best layouts for the sound source under which it was optimized. On the other hand, each of the two best layouts obtained for the aeroacoustic sound (random 4) and the monopole sound does not indicate the highest insertion loss among the five best layouts for the sound source under which it was optimized. The average value of the insertion losses for the aeroacoustic sounds (random 1–4) is also provided to estimate the noise reduction performance taking into account the change of randomness. In this case, the best layout for the aeroacoustic sound (random 2) indicates the highest average value of 19.9750 dB. The rankings of the five best layouts according to the average value of the insertion losses for the aeroacoustic sounds (random 1–4) are somewhat different from the rankings according to the insertion loss for the monopole sound.

4.3. Optimized material layouts at the combined frequencies

In this subsection, optimized material layouts at the combined frequencies are studied. The objective function is defined as Eq. (42) with the frequencies of 100 Hz, 200 Hz, and 300 Hz. Fig. 16 shows the optimization results performed at the combined frequencies for the different conditions of sound source. The optimized layouts are similar depending on the condition of sound source when the sigmoid penalty function is not applied. On the other hand, when the sigmoid penalty function is applied, the optimized layouts differ depending on the condition of sound source.

Fig. 17 shows the objective function graph and the material layouts at the different iteration numbers for one of the optimized layouts in Fig. 16. The one is the layout optimized for the aeroacoustic sound (random 1) with the sigmoid parameter s of 60. Along with the graph for the original objective function f_{obj} , the graphs for the auxiliary objective function






| | | Optimum for aeroacoustic sound (random 1) | Optimum for aeroacoustic sound (random 2) | Optimum for aeroacoustic sound (random 3) | Optimum for aeroacoustic sound (random 4) | Optimum for monopole sound |
|---|----------------------------------|---|---|---|--|---|
| | | $s=60$ | $s=50$ | $s=40$ | Non | Non |
| Best layout at combined frequencies (100 Hz, 200 Hz, 300 Hz) | |  |  |  |  |  |
| IL _{MF} at 100 Hz, 200 Hz, 300 Hz (ranking) | Aeroacoustic sound (random 1) | 16.4161 | 12.9345 | 7.2493 | 8.5870 | 9.2787 |
| | Aeroacoustic sound (random 2) | 9.8876 | 9.8018 | 6.5216 | 7.7031 | 7.9004 |
| | Aeroacoustic sound (random 3) | 8.6117 | 7.7116 | 12.4443 | 7.2109 | 7.5870 |
| | Aeroacoustic sound (random 4) | 10.5129 | 10.2936 | 6.6477 | 8.9294 | 8.8879 |
| | Average value (random 1~4) | 11.3571 (1) | 10.1854 (2) | 8.2157 (4) | 8.1076 (5) | 8.4135 (3) |
| | Monopole sound | 7.9011 (1) | 7.7288 (3) | 4.9413 (5) | 7.7552 (2) | 7.4210 (4) |

Fig. 19. Comparison between the best layouts at the combined frequencies, obtained for each condition of sound source.

f_{F_i} that represents the minus of the insertion loss at each single frequency are also provided as Eq. (45). As shown in the graphs for the auxiliary objective function, the insertion losses at the three single frequencies increase simultaneously in the early stage of iterative optimization. After the early stage, the update of material layout only increases the insertion loss at the frequency of 300 Hz.

$$f_{obj} = \frac{1}{N_F} (f_{F_1} + f_{F_2} + f_{F_3}), \quad f_{F_1} = -IL_{F_1}, \quad f_{F_2} = -IL_{F_2}, \quad f_{F_3} = -IL_{F_3} \quad (45)$$

Fig. 18 shows the postprocessed material layouts for the optimized material layouts in Fig. 16. The postprocessed layouts are characterized by the rigid materials distributed around the upper left corner of the design domain to form a reflective surface. The layouts obtained for the third aeroacoustic sound (random 3), however, do not show this characteristics well. The shapes formed by the layouts in Fig. 18 are thought to be effective in preventing the diffraction of the sound waves as well as

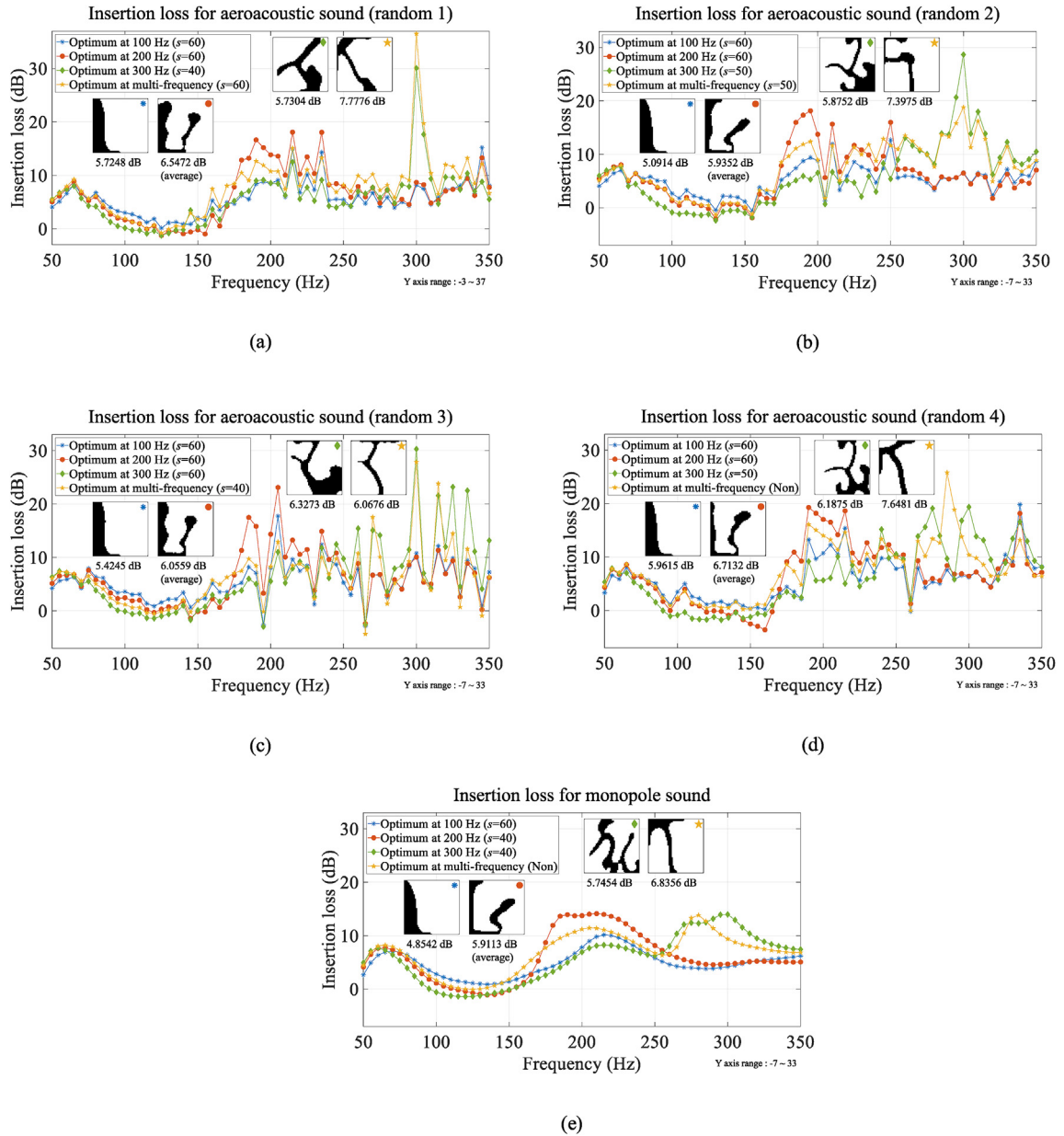


Fig. 20. Insertion loss graphs of the best layouts obtained for each condition of sound source. Results for the aeroacoustic sound sources of (a) random 1, (b) random 2, (c) random 3, and (d) random 4, along with the result for (e) the monopole sound source.

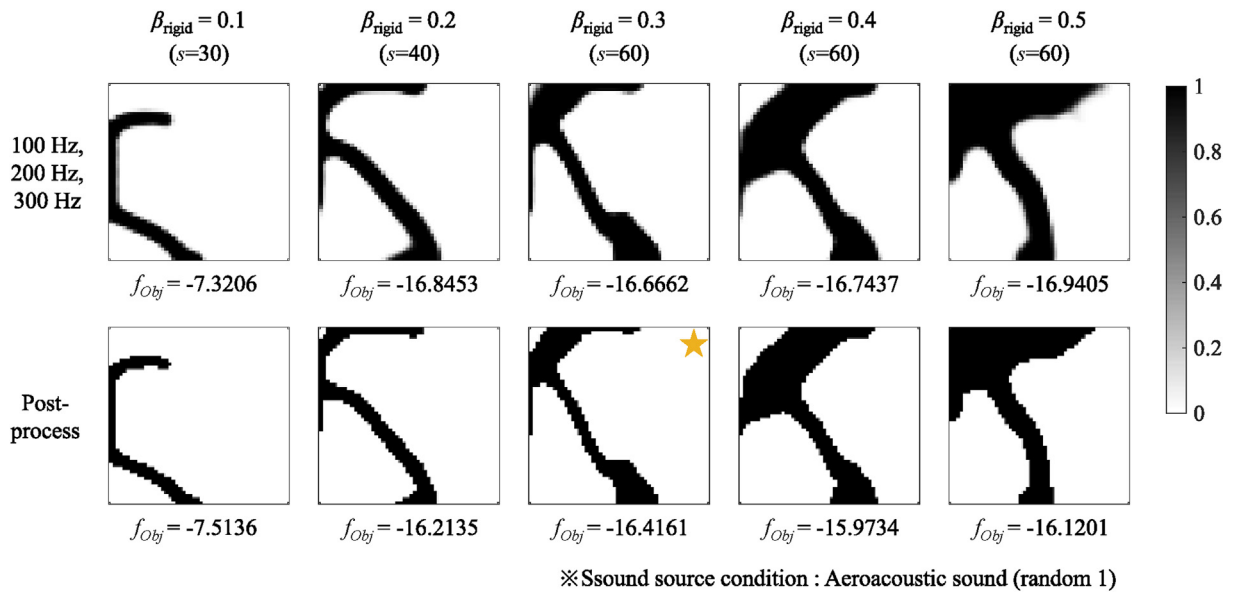


Fig. 21. Optimized material layouts and their postprocessed layouts depending on the constraint parameter β_{rigid} .

reflecting the sound waves. The layouts with a marker refer to the best layout with the lowest value of objective function among the layouts obtained under the same condition of sound source.

In Fig. 19, the insertion losses at the combined frequencies for the different random aeroacoustic sounds and the monopole sound are compared between the five best layouts at the combined frequencies, obtained for each condition of sound source. Each of the two best layouts obtained for the aeroacoustic sounds (random 1, 3) indicates the highest insertion loss among the five best layouts for the condition of sound source under which it was optimized. On the other hand, each of the three best layouts obtained for the aeroacoustic sounds (random 2, 4) and the monopole sound does not indicate the highest insertion

| | | Straight type | T-shape | T-shape with arm | Diffuser | Optimized shape |
|---|-------------------------------|---------------|------------|------------------|------------|-----------------|
| Noise barrier profiles | | | | | | |
| Number of elements | | 302 | 402 | 598 | 1382 | 633 |
| IL _{MF} at 50 Hz, 55 Hz, ... 345 Hz, 350 Hz (ranking) | Aeroacoustic sound (random 1) | 3.7141 | 7.0533 | 5.1616 | 6.4517 | 7.7776 |
| | Aeroacoustic sound (random 2) | 3.5117 | 6.8056 | 5.1020 | 6.0104 | 7.3479 |
| | Aeroacoustic sound (random 3) | 3.7084 | 6.6185 | 5.1429 | 6.0433 | 7.1365 |
| | Aeroacoustic sound (random 4) | 4.0706 | 7.4700 | 5.8492 | 6.7601 | 7.7954 |
| | Average value (random 1~4) | 3.7512 (5) | 6.9868 (2) | 5.3139 (4) | 6.3164 (3) | 7.5144 (1) |
| | Monopole sound | 3.1181 (5) | 5.8678 (2) | 4.8328 (4) | 5.8623 (3) | 6.9469 (1) |

Unit : dB

Fig. 22. Comparison of noise barrier performances between the typical top shapes and the optimized top shape.

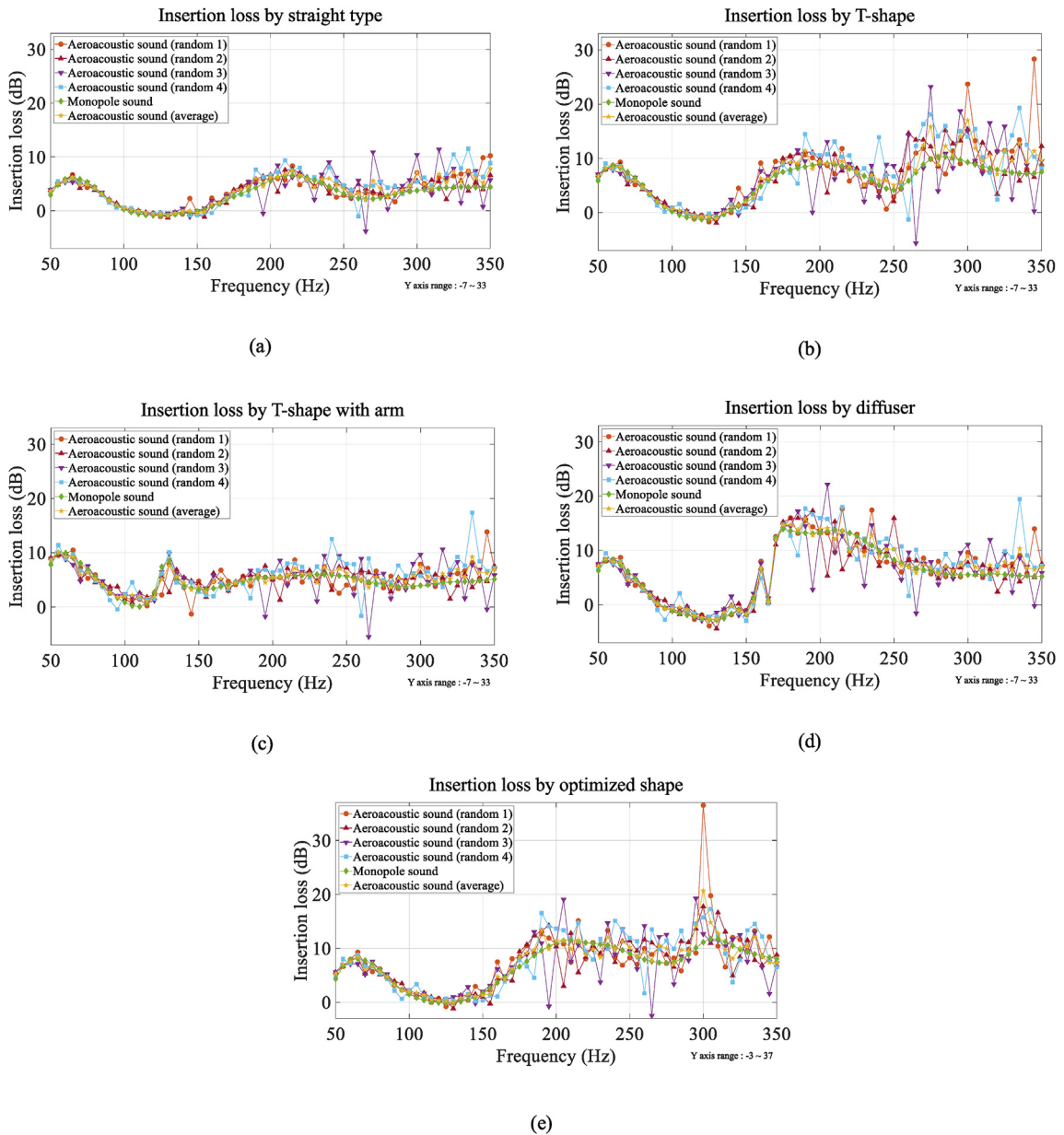
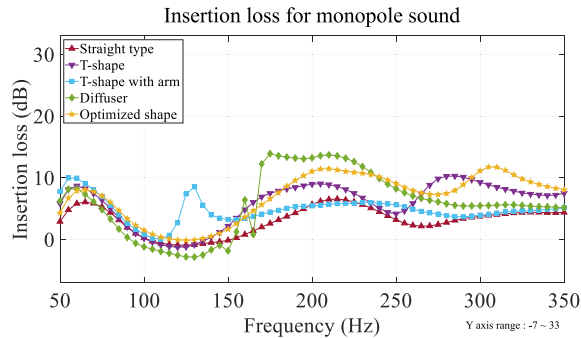


Fig. 23. Insertion loss graphs for different sound sources in each top shape. Results for (a) straight type, (b) T-shape, (c) T-shape with arm, (d) diffuser, and (e) the optimized shape.

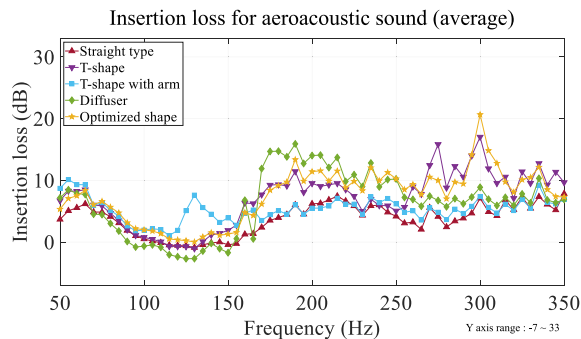
loss among the five best layouts for the condition of sound source under which it was optimized. Comparing the five layouts in terms of the average value of the insertion losses for the aeroacoustic sounds (random 1–4), the best layout for the aeroacoustic sound (random 1) indicates the highest average value of 11.3571 dB. The rankings of the five best layouts according to the average value of the insertion losses for the aeroacoustic sounds (random 1–4) are similar to the rankings according to the insertion loss for the monopole sound. If the best layout for the aeroacoustic sound (random 4) is excluded from the comparison, the rankings in both cases are the same.

The noise reduction performances of the best layouts at the combined frequencies are also analyzed through the insertion loss graph at the successive frequencies with 5 Hz intervals. Fig. 20 shows the insertion loss graphs of the best layouts at the combined frequencies with the graphs of the best layouts at each single frequency. The insertion loss graph of each best layout is calculated for the sound source that the layout was optimized for. It is found in common from the results for each sound source that the best layout at each single frequency indicates a predominant insertion loss in the frequency range near the frequency that it was optimized for. On the other hand, the best layout at the combined frequencies indicates a moderately high insertion loss over the entire frequency range from 50 Hz to 350 Hz. Comparing the best layouts in terms of the average value of the insertion losses for the entire frequency range, the best layout at the combined frequencies mostly indicates a higher value than the best layouts at each single frequency. It is known from the insertion loss graphs in Fig. 20 that the optimization results presented in Figs. 14 and 18 are appropriate.

For the optimization condition that resulted in the best layout at the combined frequencies, obtained for the aeroacoustic sound (random 1), the constraint parameter β_{rigid} in Eq. (38) needs to be changed to values other than 0.3 to find out a better layout. When the constraint parameter β_{rigid} is set to 0.1 or 0.2, the sigmoid parameter s is set to a value less than 60 due to the little reduction of the objective function value in the initial iteration stage of optimization. Fig. 21 shows the optimization results for the different values of the constraint parameter β_{rigid} . Comparing the objective function values of the postprocessed layouts in Fig. 21, the layout obtained by the constraint parameter of 0.3 indicates the lowest value of objective function.



(a)



(b)

Fig. 24. Insertion loss graphs by the typical top shapes and the optimized top shape, for (a) the monopole sound and (b) the aeroacoustic sound (average).

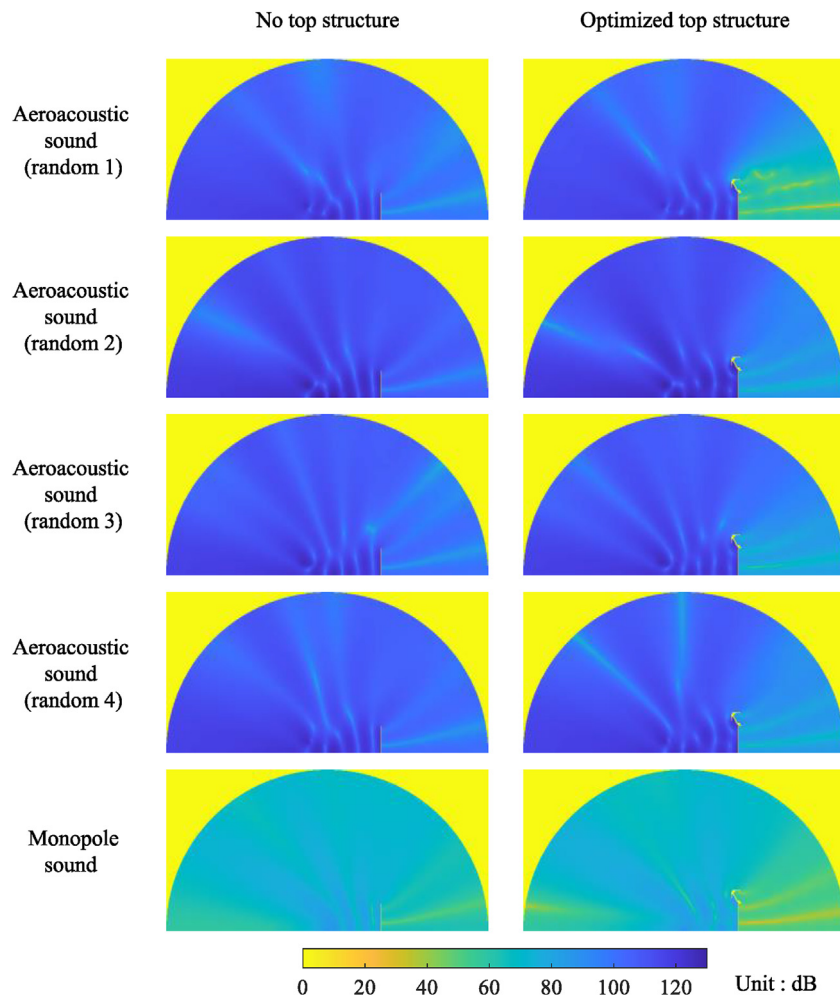


Fig. 25. Distributions of the sound pressure level for the noise barrier before and after inserting the optimized top structure.

4.4. Comparison of the optimized top shape with the typical top shapes




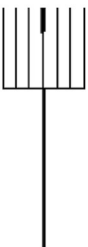

This subsection compares the noise reduction performances of the noise barrier with the optimized top shape with those of the noise barriers with typical top shapes. Fig. 22 shows the noise barrier profiles with typical top shapes and the noise barrier profile with the optimized top shape. The optimized top shape refers to the layout with a marker in Fig. 21. In Fig. 22, the insertion losses at the combined frequencies (from 50 Hz to 350 Hz with 5 Hz intervals) for the different random aeroacoustic sounds and the monopole sound are compared between the typical top shapes and the optimized top shape. Comparing these top shapes in terms of the average value of the insertion losses for the aeroacoustic sounds (random 1–4), the optimized top shape indicates the highest average value of 7.5144 dB. It also indicates the highest insertion loss of 6.9469 dB for the monopole sound. The rankings of the five top shapes according to the average value of insertion losses for the aeroacoustic sounds (random 1–4) are the same as the rankings according to the insertion loss for the monopole sound.

Fig. 23 shows the insertion loss graphs for different sound sources in each top shape. The insertion loss graph denoted by “Aeroacoustic sound (average)” means the average graph of the insertion loss graphs for the aeroacoustic sounds (random 1–4). It can be known in the results for each top shape that the mentioned average insertion loss graph (yellow line with pentagram markers) shows a quite similar fluctuation to the insertion loss graph for the monopole sound.

Fig. 24 compares the insertion loss graphs between the typical top shapes and the optimized top shape, for the same condition of sound source. In Fig. 24(a), the insertion loss graphs for the monopole sound are presented. In Fig. 24(b), the average insertion loss graphs for the aeroacoustic sounds (random 1–4) is presented. The relative performances of the five top shapes in the frequency range can be verified repeatedly in both results for the monopole sound and the aeroacoustic sound (average). In the frequency range below 150 Hz, the noise barrier named “T-shape with arm” is relatively superior to the other noise barriers. In the frequency range from 150 Hz to 250 Hz, the noise barrier named “Diffuser” is relatively superior to the others. In the frequency range above 250 Hz, the noise barriers named “T-shape” and “Optimized shape” are relatively superior to the others. In the entire frequency range from 150 Hz to 350 Hz, the noise barrier named “Optimized shape” is on average superior to the others.

Fig. 25 shows the distributions of the sound pressure level for the noise barrier before and after inserting the optimized top structure. The results are provided for the different sound sources. The frequency is 300 Hz which indicated the highest insertion loss in Fig. 24(b). The reduction of the sound pressure level is well observed in the area behind the noise barrier. The reduction is noticeable in the result for the aeroacoustic sound (random 1) like the values at 300 Hz of Fig. 23(e). The optimized top structure effectively attenuates the diffraction of sound waves to the back of the noise barrier.

Fig. 26 shows the additional comparison results for the typical top shapes and the optimized top shape with the same number of elements that make up the barrier shape. In other words, the typical top shapes in Fig. 26 are the modified shapes

| | | Straight type | T-shape | T-shape with arm | Diffuser | Optimized shape |
|--|-------------------------------|---|---|---|--|---|
| Noise barrier profiles | |  |  |  |  |  |
| Number of elements | | 633 | 633 | 633 | 633 | 633 |
| IL_{MF} at 50 Hz, 55 Hz, ... 345 Hz, 350 Hz (ranking) | Aeroacoustic sound (random 1) | 4.2607 | 6.9946 | 5.1503 | 7.1820 7.1818 (H.W.) | 7.7776 |
| | Aeroacoustic sound (random 2) | 4.0385 4.0386 (H.W.) | 6.7500 | 5.0973 | 6.6576 6.6574 (H.W.) | 7.3479 |
| | Aeroacoustic sound (random 3) | 4.2717 4.2718 (H.W.) | 6.6062 6.6063 (H.W.) | 5.1580 | 6.6833 6.6831 (H.W.) | 7.1365 |
| | Aeroacoustic sound (random 4) | 4.6620 | 7.4999 | 5.8417 | 7.3431 7.3429 (H.W.) | 7.7954 |
| | Average value (random 1–4) | 4.3082 (5) 4.3083 (H.W.) | 6.9627 (3) | 5.3118 (4) | 6.9665 (2) 6.9663 (H.W.) | 7.5144 (1) |
| | Monopole sound | 3.6203 (5) 3.6204 (H.W.) | 5.8738 (3) | 4.8249 (4) | 6.4760 (2) 6.4758 (H.W.) | 6.9469 (1) |

Unit : dB

Fig. 26. Comparison of noise barrier performances between the typical top shapes and the optimized top shape with the same number of elements that make up the barrier shape.

from the typical top shapes in Fig. 22, obtained by adjusting the area of the typical barriers to be equal to the area of the optimized barrier. After the adjustment of area, the noise barriers named “Straight type” and “Diffuser” indicate the increased insertion losses about 0.5 dB and 0.6 dB, respectively, compared with the insertion losses in Fig. 22 (refer to the values of insertion loss not written in bold type in Fig. 26). The insertion losses of the noise barriers named “T-shape” and “T-shape with arm” are not much different from the insertion losses in Fig. 22. As a result of comparing the insertion losses of the noise barriers having the same area in Fig. 26, the noise barrier named “Optimized shape” still indicates the highest insertion loss for all conditions of sound source. Fig. 27 compares the insertion loss graphs between the typical top shapes after the adjustment of area and the optimized top shape, for the same condition of sound source. The relative performances of the five top shapes in Fig. 26 are similar to the relative performances in Fig. 24, and the noise barrier named “Optimized shape” is still on average superior to the others in the entire frequency range.

The values of insertion loss (not written in bold type) in Fig. 26 represent the results by the analysis method that includes the rigid materials in the finite element domain as used for the optimization and the postprocessing. In relation to this point, it is necessary to check the values of insertion loss obtained from the analysis method that explicitly reflects the rigid structures by boundary conditions. To implement this, the hard wall boundary condition is applied to the boundaries between the noise barrier and air, and only the air domain is included in the finite element domain. The resulting values of insertion loss are written in bold type with the mark “(H.W.)” in Fig. 26. The newly calculated insertion losses (written in bold type) are almost the same as the insertion losses (not written in bold type) calculated by the analysis method presented in this study. The blank cases without the insertion loss tagged with “(H.W.)” indicate that the insertion loss is the equal for both analysis methods. Therefore, the presented values of insertion loss for the noise barriers can be accepted as the results obtained by proper simulation for the rigid materials.

5. Conclusions

In this study, topology optimization using Lighthill's equation was presented to design the top shape of noise barrier for distributed aeroacoustic sound sources. The key findings from the present optimization study were the effects of different

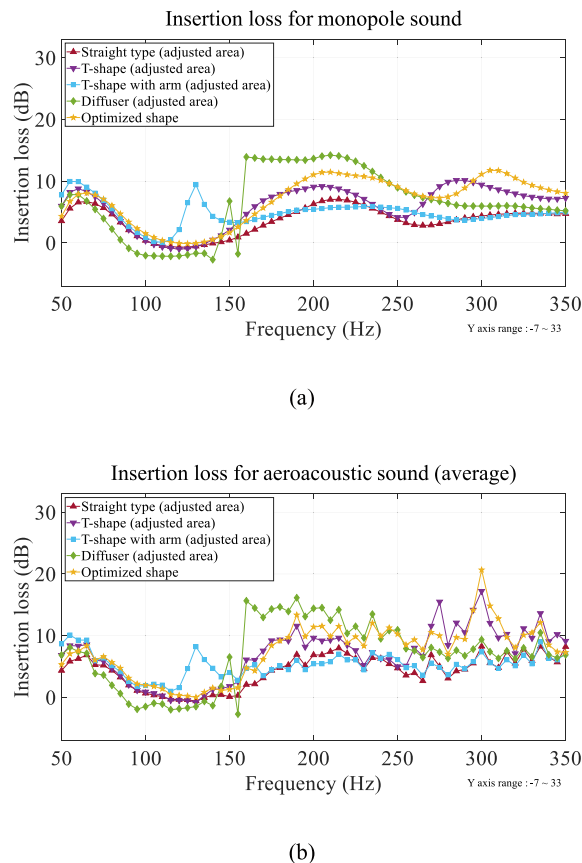


Fig. 27. Insertion loss graphs by the typical top shapes (after the adjustment of area) and the optimized top shape, for (a) the monopole sound and (b) the aeroacoustic sound (average).

random aeroacoustic sound sources, different interpolation methods, and different frequencies. First, the optimized material layout for the top shape of noise barrier was different depending on the random aeroacoustic sound source. The effect of the sound source at the single frequencies of 100 Hz and 200 Hz was small, while it was not small at the single frequency of 300 Hz and the combined frequencies including 300 Hz. But some common features were observed between the different optimized material layouts. The optimized material layouts for the simple monopole sound source also appeared somewhat different from those for the random aeroacoustic sound sources.

Second, the optimized material layout was influenced by the interpolation method. Using the sigmoid penalty function along with the linear filter resulted in various local optimums that showed visually different layouts compared to the layout obtained by using only the linear filter. For this reason, the best layout was selected among the layouts obtained under the same condition of sound source. The selected best layouts optimized under the different conditions of sound source were compared to each other by analyzing the noise reduction performances for the different random aeroacoustic sounds and the monopole sound. From the comparison results, the most reasonable layout in terms of design could be derived.

Thirdly, the optimized material layouts obtained at the single frequency or the combined frequencies proved to be satisfactory optimization results by showing superior performances in the corresponding frequency range. Although only three frequencies of 100 Hz, 200 Hz, and 300 Hz were taken into account to organize basic and systematic optimization examples, other combinations of frequencies can also be considered according to the design demand.

As far as the presented optimization examples are concerned, taking into account some random aeroacoustic sound sources can provide an optimum design which is effective for the different conditions of sound source. Therefore, an optimum design obtained only for the simple monopole sound may have limitations on the noise reduction performances for various conditions of sound source. The optimization results presented in this study may provide information for reference in the related studies.

Declaration of competing interest

The authors declare that they have no known competing financial interests or personal relationships that could have appeared to influence the work reported in this paper.

The authors declare the following financial interests/personal relationships which may be considered as potential competing interests:

CRediT authorship contribution statement

Ki Hyun Kim: Investigation, Writing - original draft. **Gil Ho Yoon:** Conceptualization, Supervision, Writing - review & editing.

Acknowledgements

This work was supported by the National Research Foundation of Korea (NRF) grant funded by the Korea government (MSIT) (NRF-2019R1A2C2084974).

References

- [1] M.P. Bendsoe, N. Kikuchi, Generating optimal topologies in structural design using a homogenization method, *Comput. Methods Appl. Math.* 71 (1988) 197–224.
- [2] M.P. Bendsoe, O. Sigmund, *Topology Optimization : Theory, Methods, and Applications*, Springer, 2003.
- [3] R.E. Christiansen, B.S. Lazarov, J.S. Jensen, O. Sigmund, Creating geometrically robust designs for highly sensitive problems using topology optimization, *Struct. Multidiscip. O* 52 (2015) 737–754.
- [4] S. Goo, S. Wang, J. Kook, K. Koo, J. Hyun, Topology optimization of bounded acoustic problems using the hybrid finite element-wave based method, *Comput. Methods Appl. Math.* 313 (2017) 834–856.
- [5] M.B. Duhring, J.S. Jensen, O. Sigmund, Acoustic design by topology optimization, *J. Sound Vib.* 317 (2008) 557–575.
- [6] J. Kook, K. Koo, J. Hyun, J.S. Jensen, S. Wang, Acoustical topology optimization for Zwicker's loudness model - application to noise barriers, *Comput. Methods Appl. Math.* 237 (2012) 130–151.
- [7] K.H. Kim, G.H. Yoon, Optimal rigid and porous material distributions for noise barrier by acoustic topology optimization, *J. Sound Vib.* 339 (2015) 123–142.
- [8] W.C. Zhao, L.L. Chen, C.J. Zheng, C. Liu, H.B. Chen, Design of absorbing material distribution for sound barrier using topology optimization, *Struct. Multidiscip. O* 56 (2017) 315–329.
- [9] J.W. Lee, Y.Y. Kim, Topology optimization of muffler internal partitions for improving acoustical attenuation performance, *Int. J. Numer. Methods Eng.* 80 (2009) 455–477.
- [10] G.H. Yoon, Acoustic topology optimization of fibrous material with Delany-Bazley empirical material formulation, *J. Sound Vib.* 332 (2013) 1172–1187.
- [11] E. Wadbro, M. Berggren, Topology optimization of an acoustic horn, *Comput. Methods Appl. Math.* 196 (2006) 420–436.
- [12] L.R. Lu, T. Yamamoto, M. Otonari, T. Yamada, K. Izui, S. Nishiwaki, Topology optimization of an acoustic metamaterial with negative bulk modulus using local resonance, *Finite Elem. Anal. Des.* 72 (2013) 1–12.
- [13] G.H. Yoon, J.S. Jensen, O. Sigmund, Topology optimization of acoustic-structure interaction problems using a mixed finite element formulation, *Int. J. Numer. Methods Eng.* 70 (2007) 1049–1075.
- [14] G.H. Yoon, H. Choi, S. Hur, Multiphysics topology optimization for piezoelectric acoustic focuser, *Comput. Methods Appl. Math.* 332 (2018) 600–623.
- [15] S. Oh, S. Wang, S. Cho, Topology optimization of a suction muffler in a fluid machine to maximize energy efficiency and minimize broadband noise, *J. Sound Vib.* 366 (2016) 27–43.

- [16] K.S. Oh, J.W. Lee, Topology optimization for enhancing the acoustical and thermal characteristics of acoustic devices simultaneously, *J. Sound Vib.* 401 (2017) 54–75.
- [17] J.K. Guest, J.H. Prevost, T. Belytschko, Achieving minimum length scale in topology optimization using nodal design variables and projection functions, *Int. J. Numer. Methods Eng.* 61 (2004) 238–254.
- [18] K. Svanberg, H. Svard, Density filters for topology optimization based on the Pythagorean means, *Struct Multidiscip O* 48 (2013) 859–875.
- [19] O. Sigmund, Morphology-based black and white filters for topology optimization, *Struct Multidiscip O* 33 (2007) 401–424.
- [20] M.J. Lighthill, On sound generated aerodynamically .1. General theory, *Proc R Soc Lon Ser-A* 211 (1952) 564–587.
- [21] M.J. Lighthill, On sound generated aerodynamically .2. Turbulence as a source of sound, *Proc R Soc Lon Ser-A* 222 (1954) 1–32.
- [22] B.E. Laufer, D.B. Spalding, The numerical computation of turbulent flows, *Comput. Methods Appl. Math.* 3 (1974) 269–289.
- [23] W. Bechara, C. Bailly, P. Lafon, S.M. Candel, Stochastic approach to noise modeling for free turbulent flows, *AIAA J.* 32 (1994) 455–463.
- [24] T. Ishizuka, K. Fujiwara, Performance of noise barriers with various edge shapes and acoustical conditions, *Appl. Acoust.* 65 (2004) 125–141.
- [25] M.R. Monazzam, Y.W. Lam, Performance of profiled single noise barriers covered with quadratic residue diffusers, *Appl. Acoust.* 66 (2005) 709–730.
- [26] R. Toledo, J.J. Aznarez, D. Greiner, O. Maeso, Shape design optimization of road acoustic barriers featuring top-edge devices by using genetic algorithms and boundary elements, *Eng. Anal. Bound. Elem.* 63 (2016) 49–60.
- [27] D. Duhamel, Shape optimization of noise barriers using genetic algorithms, *J. Sound Vib.* 297 (2006) 432–443.
- [28] M. Baulac, J. Defrance, P. Jean, Optimisation with genetic algorithm of the acoustic performance of T-shaped noise barriers with a reactive top surface, *Appl. Acoust.* 69 (2008) 332–342.
- [29] G.H. Yoon, Y.Y. Kim, The role of S-shape mapping functions in the SIMP approach for topology optimization, *KSME Int. J.* 17 (2003) 1496–1506.
- [30] K. Svanberg, The method of moving asymptotes - a new method for structural optimization, *Int. J. Numer. Methods Eng.* 24 (1987) 359–373.
- [31] M.E. Goldstein, *Aeroacoustics*, McGraw-Hill International Book Co., New York, 1976.
- [32] R.H. Kraichnan, Diffusion by a random velocity field, *Phys. Fluids* 13 (1970), 22–+.
- [33] M. Karweit, P. Blanckenon, D. Juve, G. Comtebellot, Simulation of the propagation of an acoustic-wave through a turbulent velocity-field - a study of phase variance, *J. Acoust. Soc. Am.* 89 (1991) 52–62.
- [34] M. Billson, L.E. Eriksson, L. Davidson, Jet Noise Prediction Using Stochastic Turbulence Modeling, 9th AIAA/CEAS Aeroacoustics Conference, South Carolina, 2003.
- [35] M. Mesbah, J. Meyers, M. Baelmans, W. Desmet, Assessment of Different Parameters Used in the SNGR Method, 2004. ISMA2004.
- [36] C. Bailly, D. Juve, A stochastic approach to compute subsonic noise using linearized Euler's equations, in: 1999 American Institute of Aeronautics & Astronautics, 1999.
- [37] C. Bailly, P. Lafon, S. Candel, Computation of noise generation and propagation for free and confined turbulent flows, in: AIAA/CEAS Aeroacoustics Conference, Pennsylvania, 1996.
- [38] P. Francescantonio, Assessment of SNGR method for robust and efficient simulations of flow generated noise, in: 19th AIAA/CEAS Aeroacoustics Conference, Berlin, 2013.
- [39] A. Lafitte, E. Laurendeau, A study based on the sweeping hypothesis to generate stochastic turbulence, in: 9th AIAA/CEAS Aeroacoustics Conference, Portland, 2011.
- [40] Y.H. Pao, Structure of turbulent velocity and scalar fields at large wavenumbers, *Phys. Fluids* 8 (1965) 1063–&.
- [41] J.W. Lee, Y.Y. Kim, Rigid body modeling issue in acoustical topology optimization, *Comput. Methods Appl. Math.* 198 (2009) 1017–1030.